Study of Surface Quantum Wells in InSb/AlInSb Heterostructures

by

Emma Annelise Bergeron

A thesis
presented to the University of Waterloo
in fulfillment of the
thesis requirement for the degree of
Master of Science
in
Physics

Waterloo, Ontario, Canada, 2019

Author's Declaration

I hereby declare that I am the sole author of this thesis. This is a true copy of the thesis, including any required final revisions, as accepted by my examiners.

I understand that my thesis may be made electronically available to the public.

Abstract

The strong spin orbit coupling and large Lánde g-factor of InSb compared to the other III-V semiconductors makes InSb an ideal choice for potential use in topological quantum computing with Majorana fermions. Furthermore, two dimensional electron gases (2DEGs) in III-V materials offer a more scalable platform for topological quantum computing over nanowire networks. Despite their ideal properties, 2DEGs in InSb have not been exploited for the purpose of studying Majorana fermions due to outstanding materials development challenges.

This thesis presents an investigation of InSb/$Al_xIn_{1-x}Sb$ heterostructures including surface quantum wells and standard high electron mobility transistor (HEMT) heterostructures. Development of fabrication methods and techniques is discussed for each system. Transport is characterized through mangetotransport measurements including quantum Hall effect and Shubnikov de-Haas oscillations. We extract carrier densities and mobilities for a series of wafers of varying doping densities. Gated structures allow further modulation of the carrier density and characterization of the effectiveness of gating is reported.

Acknowledgements

I owe my sincerest thanks to everyone who has helped me in the pursuit of higher education. I would like to thank specifically my professor Dr. Jonathan Baugh for giving me the opportunity to pursue this research project and for the guidance he has provided along the way. I would also like to give special thanks to Dr. Francois Sfigakis for the tireless support and hands on training that has helped me develop the skills of a true experimentalist. Additionally, I owe my gratitude to all the staff of the University of Waterloo nanofab facility for making it the renown facility that it is today and for going above and beyond to make sure the needs the nanofab community are met. On that note, I also want to extend thanks to Mike and Ophelia Lazaridis for their investment in Waterloo and for their investment in me through the Mike and Ophelia Lazaridis fellowship that made pursuing this degree possible.

I'm grateful for the many friends I have made since my move to Waterloo. My roomie turned best friend Priyanka Ball for her endless emotional support, my good friend Vinay Guthal who partakes in or instigates all of my misadventures, my Canadian family the Huegles who have adopted and supported me since literally my first morning in Canada and especially all of my coworkers at RAC who have made every day enjoyable, even the troubling times when samples may or may not be functioning.

To the friends who got me here, especially Cedric Williams, I owe you all the thanks in the world for giving me the confidence to pursue my dreams. I'm so glad to have had another southerner in the north to commiserate with all winter long.

Finally, I want to thank my family for loving and supporting me in my every single endeavor. I love you Mom, Dad, Chloe, Corey, and Maw Maw. You mean the world to me.

Dedication

This is dedicated to my beloved pup, Roux.

Table of Contents

List of Tables

List of Figures

Chapter 1

Introduction

1.1 Motivation

InSb has the smallest effective electron mass, the smallest band gap and the highest room temperature electron mobility of all the binary III-V semiconductors (78,000 cm^2/Vs). Combined with strong spin-orbit coupling and a large Lánde g-factor (-51 in bulk InSb), InSb quantum wells are ideal heterostructures for high performance spintronic and electronic devices. Recent achievements in developing systems hosting Majorana bound states (the condensed matter equivalent of Majorana Fermions) have motivated the development of Majorana based topological quantum computing.

The proposal for a system hosting Majorana bound states requires a 1D semiconducting quantum wire with large spin orbit coupling and proximity induced superconductivity in the presence of a perpendicular magnetic field [**?**]. In 2012 the first reported signatures of Majorana bound states were produced in gated InSb nanowire-superconductor devices[**?**]. Several groups have since reported on improved systems and more robust signatures of Majorana modes in InAs [**?**][**?**] and InSb nanowires [**?**]. Due to the difficulty in creating larger device networks from as-grown nanowires, such as topological qubits, attention has turned to the use of two dimensional electron gases (2DEGs) for creating these devices through top down fabrication processes. It has been shown in InAs 2DEGs that effectively 1D etched quantum wires are indeed capable of producing Majorana devices [**?**][**?**].

To date, InSb systems have not progressed to the point of InAs systems due to numerous growth and fabrication challenges. These challenges are the focus of the current work and will be discussed in detail in the following chapters. InSb/AlInSb quantum

wells have reported electron mobilities up to 350,000 cm^2/Vs though these systems generally report parallel conduction making them difficult to properly gate the carrier density [?][?][?][?][?][?]. Thus, these systems are not suitable for most spintronic and electronic applications that require gating of the 2DEG to pinchoff (zero current), as is the case with forming a quantum point contact. In fact, only two reports have shown successful gating of InSb quantum wells to pinchoff [?][?]. Generally, reports of high electron mobilities in InSb/AlInSb quantum wells have been for standard high electron mobility transistors (HEMTs) where mobility is enhanced by burying the quantum well beneath the doped barrier layer protect it from impurities, surface states and crystal defects at the surface. However, HEMTs intended for use in developing Majorana devices require the quantum well to lie at the *surface* of the structure so that the quantum well inherits the properties of a superconductor deposited on the surface, an effect known as proximity induced superconductivity. Such structures are known as "inverted" HEMTs where the quantum well is grown above the doped barrier layer. These surface quantum wells are plagued by disorder from the surface and are more difficult to gate due to shielding of the doping layer by the quantum well. A report of the first surface quantum well was published this year and reports a quantum well mobility of 107,000 cm^2/Vs for an inverted HEMT located 50nm below the surface by an undoped barrier layer for enhanced mobility. Though by far the most competitive structure for pursuing InSb 2DEG based Majorana devices to date, the 50nm top barrier would pose a problem in pursuing proximity induced superconductivity. The structures reported in this thesis, to the best of my knowledge, serve as the first reports of a true *surface* quantum well in an InSb/AlInSb heterostructure.

1.2 Thesis at a glance

The following sections outline our preliminary work in developing an InSb quantum well heterostructure motivated by recent interest in the field to pursue scalable topological quantum computing with Majorana bound states. Chapter 2 outlines the necessary background solid state physics concepts for understanding III-V crystal structures and the unique electrical properties that arise when electrons are confined to reduced dimensions in heterostructures of these materials. A section on heterostructure design explains the physical realization of these systems through band gap engineering and advancements in molecular beam epitaxy (MBE). The chapter concludes by providing an explanation of the unique transport phenomena associated with 2DEGs, the effect and Shubnikov de-Haas (SdH) oscillations. Further background information is given in subsequent chapters when necessary. The first part of chapter 3 introduces the InAs and InSb heterostructures

studied in this work and discusses design choices and relevant issues with MBE growth. The second part outlines the nanofabrication process used to create devices from 2DEGs. Chapter 4 overviews our measurement setup and presents the transport data that constitutes the main contributions of this work. Appendix A provides photoresist recipes not provided in the main text and appendix B contains supplemental transport data.

Chapter 2

Basic Concepts

2.1 Narrow gap III-V semiconductors

2.1.1 Crystal properties

One of the most basic properties that defines a crystal is the lattice structure. Just like a 3D grid, every lattice point (grid point) in a crystal is an integer translation from any other lattice point by a given set of three vectors. Additionally each lattice point in a crystal is identical, meaning the same arrangement of composite atoms are present at each location. This fundamental repeating arrangement of atoms is referred to as the unit cell of the crystal and can take different geometries, referred to as the Bravais lattices. There are fourteen Bravais lattices, but the most common structure for semiconductor crystals is the cubic cell which has sides of all equal length, a, and all angles equal to 90°. The cubic unit cell includes three possible arrangements of atoms: the simple cubic, the face centered cubic (fcc), and the body centered cubic (bcc). The simple cubic contains atoms at all eight vertices of the cube, the fcc contains an additional atom at the center of each face of the cube, and the bcc contains one additional atom at the center of the cube. For III-V materials like InAs or InSb, the crystal structure is formed from two inter-penetrating fcc lattices (one for each atomic species) often referred to as a zinc-blend structure shown in figure **??**a. Zinc-blend structures have inversion asymmetry, which provides them with electrical and optical properties that are advantageous over monatomic materials like Si. Notably, this inversion asymmetry produces spin orbit interaction in the material.

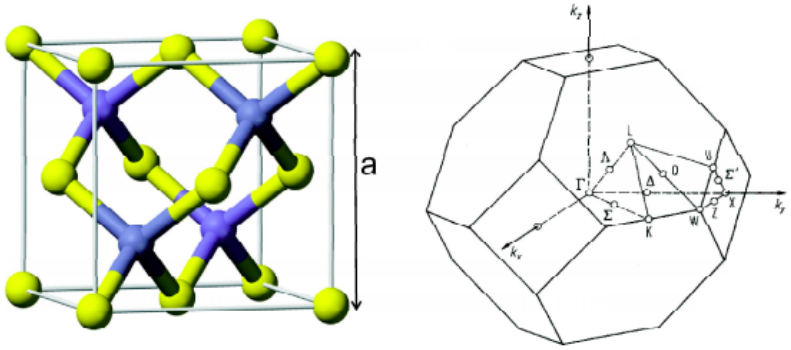

Figure 2.1: (a) Unit cell of a III-V zinc blende crystal structure in real space. The colors denote the differing atomic species of the compound. In the case of InSb, In (Sb) is shown in blue (green). (b) Wigner-Seitz cell of InSb in reciprocal space with axes k_x, k_y, and k_z ([100], [010], [001]). Remaining directions in k-space are given by Δ, Σ, and Λ ([010], [110], and [111]). The Γ point corresponds to zero momentum. The symmetry points K, L, U, X correspond to symmetry points under rotation and reflection about the Γ point. Figures reused from [**?**].

The behavior of electrons in a material is determined by the distribution of available electron states, known as the bandstructure (a plot of energy versus momentum). The difference in bandstructure between metals, semiconductors and insulators is the reason for the very different electrical properties of each of these classifications of materials. Studying the bandstructure of a crystal lattice requires translating the lattice from real space to momentum space where it's known as the reciprocal lattice. In reciprocal space, the unit cell is known as the Wigner-Seitz cell or the first Brillouin zone and provides useful information about the bandstructure of the material. As seen in figure **??**b, the Wigner-Seitz cell in reciprocal space reveals the important symmetry points relative to the center of the cell. Due to the periodicity of the reciprocal lattice, any point k' outside the first Brillouin zone can be mapped to an equivalent point k within the first Brillouin zone. Therefore when determining bandstructure it is sufficient to determine the energies of each band within the first Brillouin zone only.

2.1.2 Electrical properties

In the free electron model, a simple parabolic energy band, $E = \hbar^2 k^2/2m$, results from the solution of the Schrödinger equation for a single electron modeled by a standing wave,

$\Psi_k(r) = e^{ikr}$. The behavior of electrons in a crystal structure, however, is modeled through the nearly-free electron model [**?**]. The addition of a periodic potential $V(r)$ to the Hamiltonian models the effects of the ion cores in the crystal lattice. The Schrödinger equation for an electron in a periodic potential is given by

$$(\frac{-\hbar^2}{2m^*}k^2 + V(r))\Psi_k(r) = E_k\Psi_k(r), \tag{2.1}$$

where $\hbar$ is the reduced Planck constant, m^* is the effective mass, E_k is the energy of a given momentum state, and k is the momentum. It is then solved according to Bloch's theorem where Bloch wave functions are periodic functions, $v_k(r + a) = v_k(r)$, modulated by a plane wave with a longer period given by

$$\Psi_k(r) = v_k(r)e^{ikr} \tag{2.2}$$

where $v_k(r)$ depends on the wave vector.

The presence of a periodic potential causes energy gaps to appear in the parabolic band structure at values of $k = n\frac{\pi}{a}$ where n is an integer and a is the periodicity of the potential. Each continuous region of the bandstructure forms an allowed band that repeats every $2\pi/a$. A plot of the allowed bands is generally shown in a reduced form discussed previously as the first Brillouin zone, the region from $-\pi/a \leq k \leq \pi/a$. A plot of the bandstructure of an electron in the free electron model and the nearly-free electron model is seen in figure **??**.

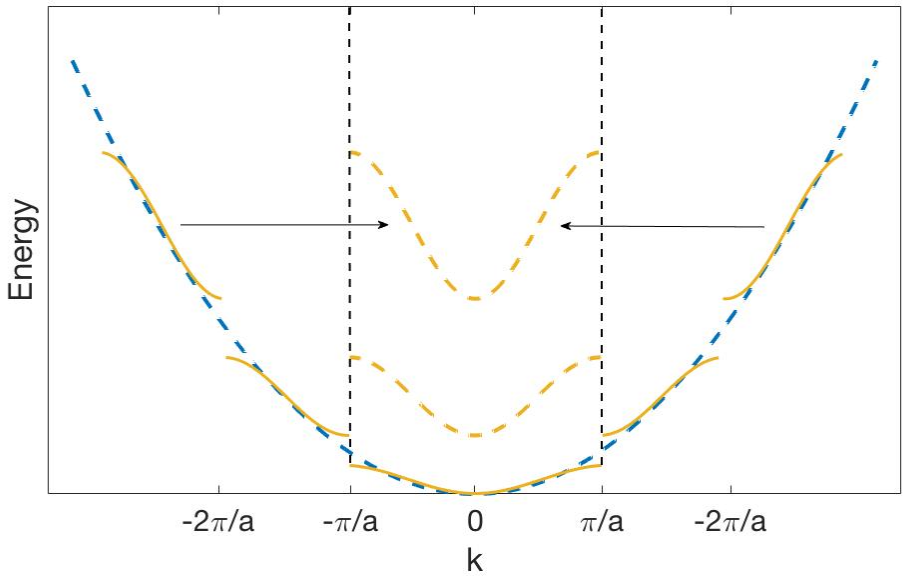

Figure 2.2: Parabolic band-structure for the free electron model in one dimension (dashed) and nearly-free electron model (solid) showing band gaps. The first Brillouin zone is marked by vertical dashed lines with the reduced zone form of the bands shown.

In order to calculate the full band structure of a material with many bands, a more comprehensive technique is required over the nearly free electron model. There have been many techniques used in calculating the full bandstructure of III-V compounds, including the pseudo-potential method which is shown in figure **??** [**?**]. As seen at $\Gamma(k = 0)$, the conduction band minima and the valence band maxima occur at the same point proving InSb to be a direct band gap material. In considering the region in energy and momentum near the band gap, it is reasonable to describe the bandstructure using 4 bands given all other bands are well separated in energy. This includes the conduction band and the heavy hole, light hole, and split-off valence bands shown figure **??**.

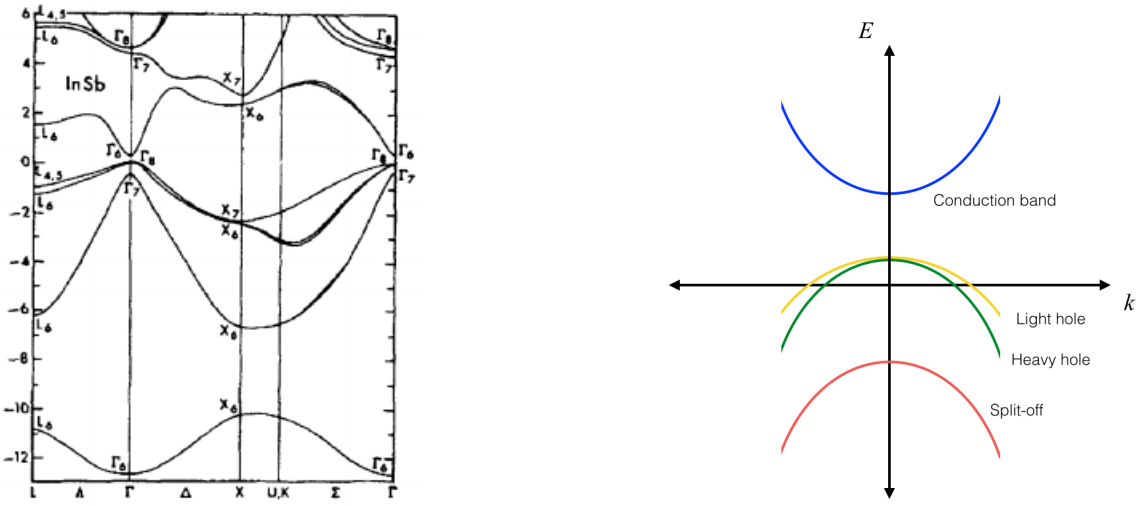

(a) (b)

Figure 2.3: A plot of (a) the complete bandstructure of InSb using the psuedo potential technique, reused with permission from [**?**], and (b) a schematic of the effective mass approximation of the four bands near the Γ point ($k = 0$) in figure (a).

Thus, a simpler method than the psuedo-potential technique can be used to model the bandstructure as just these four bands. For small values of k where nonparabolicity is insignificant, the effective mass approximation (EMA) is sufficient. Because the model approximates the bands as parabolic, electrons (holes) do not feel the presence of other bands and thus reside exclusively in the conduction (valence) band. The solution to the Schrödinger equation in this case is given by

$$E(k) = E_0 + \frac{\hbar^2 k^2}{2m^*} \tag{2.3}$$

where E_0 is the energy of the band edge and m^* is the effective mass.

For narrow-gap semiconductors like InSb, the band-structure is known to get increasingly non-parabolic for increasing values of k. In this case, the bands can no longer be approximated as parabolic as in the EMA. Instead, the most commonly used model which accounts for this non-parabolicity is the eight band Kane model [**?**]. In this model the Hamiltonian is given as a matrix that includes inter-band tunneling which is more significant for materials with smaller band gaps. A schematic comparing the band dispersion for EMA and the eight band Kane model is given in figure **??**.

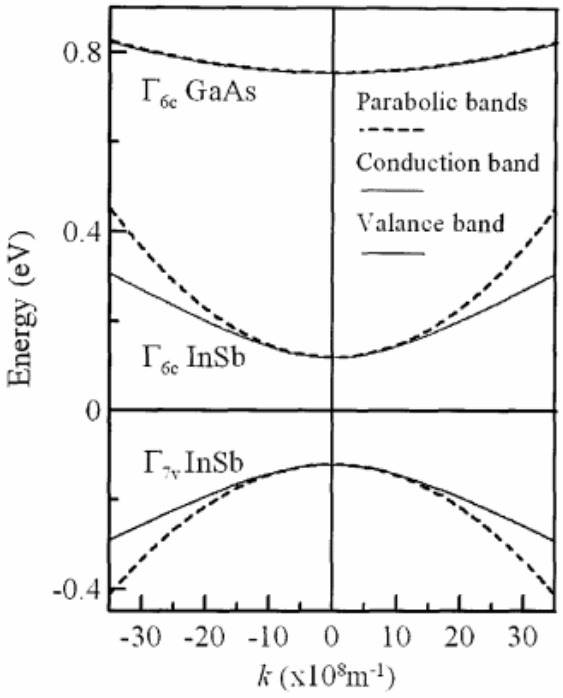

Figure 2.4: Band dispersion relationship as calculated using the effective mass approximation (EMA) (dashed) and the eight band Kane model (solid). Reused from [**?**].

2.2 Two-dimensional electron gases

2.2.1 Confinement in 2D

The density of states of a system is the number of available electron (or hole) states per unit volume as a function of energy. The allowed wavevectors are determined from solving the "particle in a box" analogy for electrons confined in a crystal lattice where particle wavefunctions must satisfy the boundary conditions of the crystal. The allowed k_x, k_y, and k_z wave-vectors form a grid in k-space. The number of states encapsulated in a spherical shell of diameter k and width dk gives the density of states as a function of k. A 2D cross section of a spherical shell in k-space is depicted in figure **??**. The function can be rewritten as a function of energy using the fundamental relations between wavevector, momentum p, and energy E. The resulting 3D density of states as a function of energy is

$$g_{3D}(E) = \frac{m^*[2m^*(E - E_c)]^{1/2}}{\pi^2\hbar^3} \tag{2.4}$$

where m^* is the effective mass, $\hbar$ is planck's constant, and $E - E_c$ is the energy relative to the minimum of the conduction band (fig. **??**a).

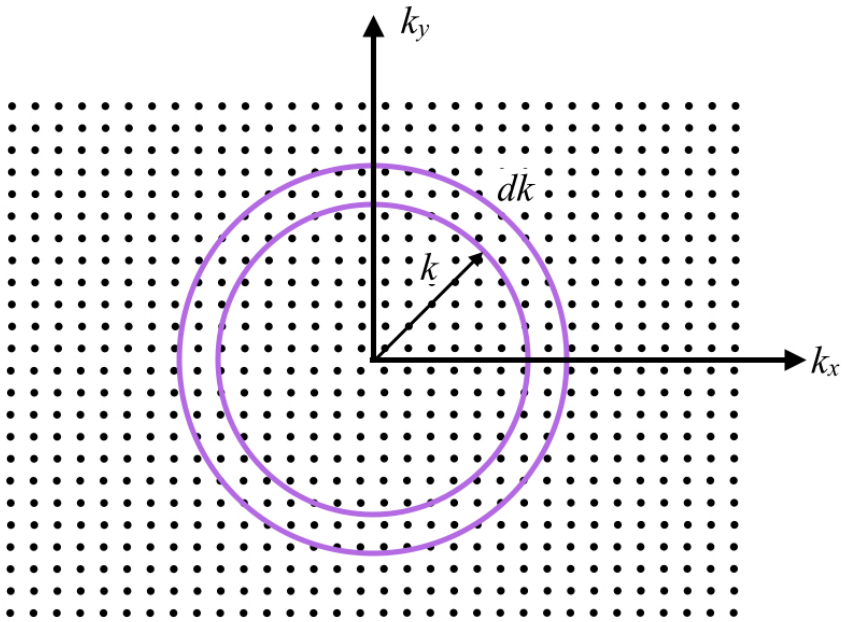

Figure 2.5: 2D cross section of a spherical shell in k-space with inner diameter k and thickness dk.

Confining the motion of electrons to 2D, results in a $k_z = 0$ wavevector. The density of states in k-space is then determined by the number of states encapsulated in a ring of diameter k and width dk in the $k_x - k_y$ plane. Similar to the 3D case, the 2D density of states can be rewritten in terms of energy yielding the relation

$$g_{2D}(E)dE = \frac{m^*dE}{\pi\hbar^2} \tag{2.5}$$

which is, remarkably, independent of energy E. The significance of this result is that as soon as the Fermi level rises above the conduction band edge, the number of states becomes proportional to E_F - E_c. In reality, however, confinement in 2D is better classified as *quasi*-2D meaning $k_z = \pi n/w$ where n is the subband index of the quantum well and w is the width of the quasi-2D well. The density of states then becomes a step function,

$$g_{2D}(E) = \sum_{n_z} \frac{m^*}{\pi\hbar^2}\theta(E - E_{n_z}), \tag{2.6}$$

where new states become available at the start of each new subband (fig. **??**b).

Further confinement of a quantum well into 1D results in an $E^{-1/2}$ dependence of the density of states in each subband. For the first subband, this is given by

$$g_{1D}(E) = \frac{2}{\pi\hbar}\left[\frac{2m^*}{(E - E_c)}\right]^{1/2} \tag{2.7}$$

with a step-like jump in the number of states for each new subband (fig. **??**c).

In the case of a quantum dot, no free motion of the electron is possible. The electron, confined to exist as a quasi zero-dimensional object, has no net momentum. As such, in *quasi*-0D, available states only exist at discrete energies described by a delta function (fig. **??**d),

$$g_{0D}(E) = 2\delta(E - E_c). \tag{2.8}$$

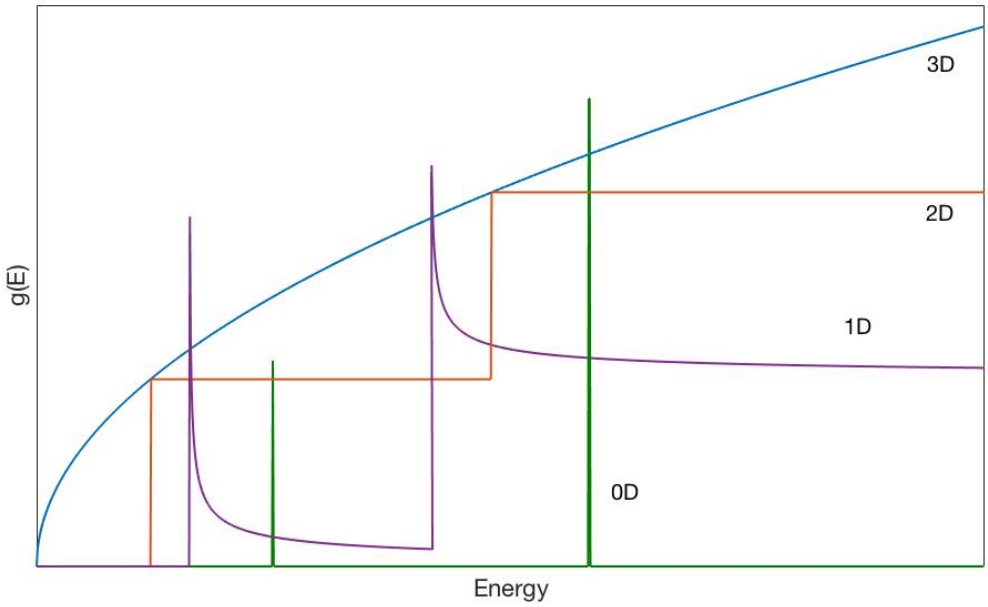

Figure 2.6: Density of states (DOS) as a function of energy for 3D, 2D, 1D and 0D systems.

2.2.2 Time and length scales of confined systems

From a discussion of the density of states, the effects of confinement are made apparent but the ability to confine an electron depends on certain material parameters. This is determined by the Fermi wavelength λ_F of the system. In order for quantum effects to arise, the physical length scale of confinement must be on the order of the Fermi wavelength defined by

$$\lambda_F = \frac{2\pi}{k_F} = \sqrt{\frac{2\pi}{n_{2D}}}, \tag{2.9}$$

where k_F is the Fermi wavevector in 2D and n_{2D} is the 2D carrier density of the quantum well. If this condition does not hold, the required discreteness of available energy states in the confined dimension will smear out and result in bulk transport.

This explains why semiconductor material systems are ideal for designing quantum well heterostructures since their carrier densities are small enough (compared to metals) to yield λ_F on the order of achievable quantum well dimensions of 10 - 100 nm. Additionally, the Fermi energy is dependent on this wavelength by

$$E_F = \frac{(2\pi\hbar)^2}{2m\lambda_F^2}. \tag{2.10}$$

For semiconductors with carrier densities on the order of 10^{15} m^{-2}, Fermi energies are less than 10 meV.

Quality of transport is determined by ease with which an electron travels through the material. The mean free path is the average distance an electron travels between successive collisions with impurities or defects in the material. The mean free path is given by

$$l = v_F\tau, \tag{2.11}$$

where v_F is the Fermi velocity and τ is the momentum relaxation time or the time between successive collisions. These parameters distinguish the material as being in one of two transport regimes: ballistic if $l >> L$ or diffusive if $l << L$ where L is the length scale over which transport is measured. A metric typically used to describe the quality of a quantum well is the mobility, $\mu = e\tau/m^*$, from which the momentum relation time and mean free path of electrons can be determined. Further details on experimentally determining mobility are given in section 2.4 on magnetotransport.

2.3 Heterostructure Design

2.3.1 Band gap engineering

In materials science, Vergard's law is the rule of thumb for varying the electrical properties of a compound through alteration of its chemical composition. Vergard's law is given by $a_{AB} = (1-x)a_A + xa_B$ where a_A and a_B are the lattice constants of the constituent materials, a_{AB} is the lattice constant of the compound and x is the molar fraction of material B. The law states that material parameters of the compounds such as lattice constant, band gap, and dielectric constant vary linearly with alloy composition x. In reality, not all compositions obey the rule of linearity but Vergard's law remains a good approximation, especially when no other information is known about a system. The variation in band gap as a function of lattice constant for common III-V compounds is given in figure **??**.

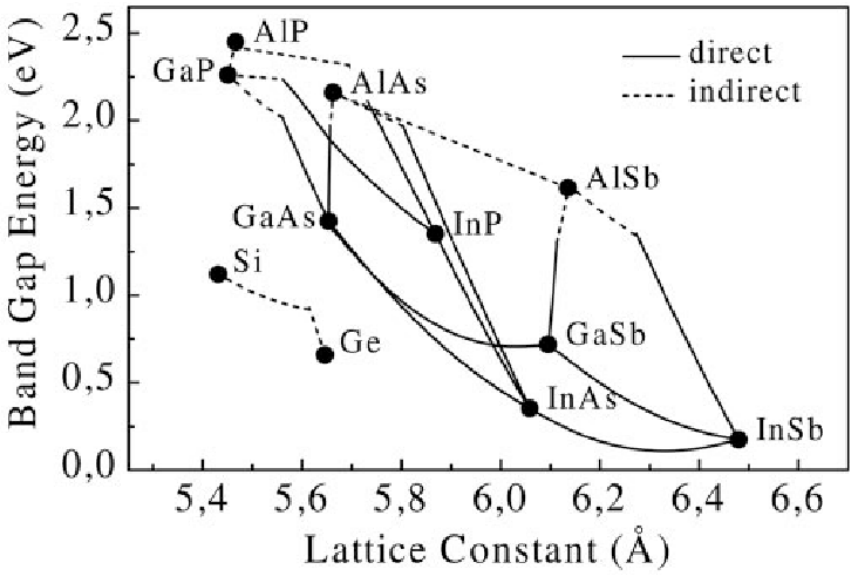

Figure 2.7: Bandgap as a function of lattice constant for the common III-V binary compounds (dots). The relation for bandgap of ternary compounds as a function of chemical composition is given by the lines between binary compounds. Dotted (dashed) lines refer to direct (indirect) band gaps, some are very linear (AlInSb) obeying Vergard's law while others are more curved (InGaAs). Taken from [**?**].

From this law, band gap engineering has advanced the development of low dimensional systems through the engineering of quantum wells at the interface of lattice matched materials of differing band gaps, known as heterojunctions (fig. **??**). Molecular beam epitaxy (MBE) is a method of growing atomically pristine semiconductor crystals and has allowed for the defect free growth of these heterojunctions. Take for example the now commonly used GaAs/Al_xGa_{1-x} system. GaAs and AlAs are nearly lattice matched, meaning the lattice matching of a GaAs/Al_xGa_{1-x}As heterojunction will not depend on the aluminum content. For InSb/Al_xIn_{1-x}Sb systems, however, InSb and AlSb have very different lattice constants. In this case, the lattice matching of InSb/Al_xIn_{1-x}Sb will strongly depend on the concentration of aluminum leading to some amount of lattice mismatch. The strain caused in the crystal by the differing lattice constants will cause defects in the growth of these structures, which could lead to delamination of layers in the worst case. Thus optimizing the growth of such systems is an ongoing area of research in MBE.

2.3.2 Modulation doping

Modulation doping is the method of introducing dopants into the higher band gap material of a quantum well heterostructure where they are separated from the quantum well by an undoped spacer layer. Due to this separation, the donors' contribution to scattering in the quantum well is much reduced, which has led to extremely high electron mobilities in modulation doped structures. Modulation doping also eliminates the issue of dopant freeze-out at cryogenic temperatures, a phenomenon in which the charge carriers remain localized to donors [**?**]. The large difference in band gap between the donor ions and the charge carriers in the lower lying quantum well prevents the charge carriers from being trapped at cryogenic temperatures. The result of this separation also creates an electric field which critically influences the bandstructure. The effect is known as band bending and is illustrated in figure **??**.

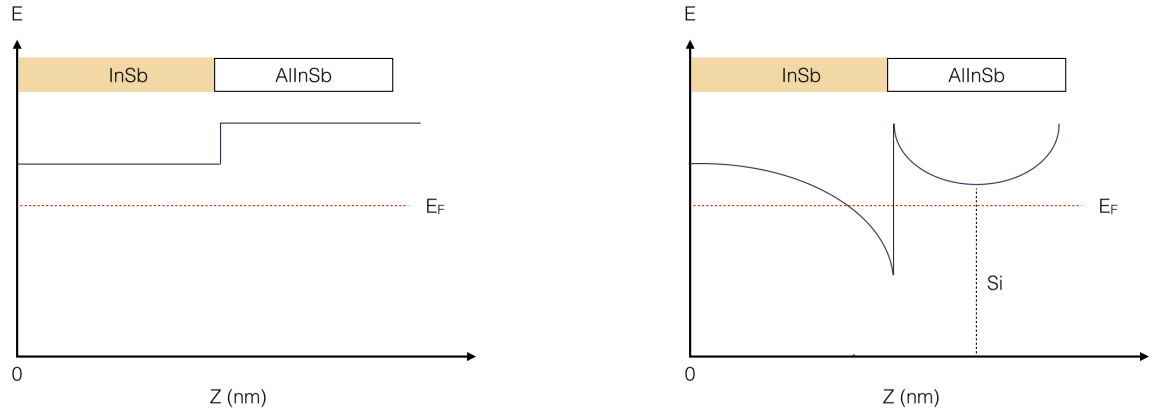

Figure 2.8: (a) Schematic of the conduction band diagram for an (a) undoped InSb/AlInSb heterostructure showing the differing bandgaps of the materials and (b) a modulation n-doped heterostructure with the resultant band bending forming a quantum well. Silicon, Si, is a common n-type dopant for InSb/AlInSb heterostructures. A vertical dotted line denotes the position of the Si δ-doping plane with respect to the depth of the quantum well, Z, along the x-axis. A populated 2DEG requires the Fermi level, E_F (horizontal dotted line), to be above the minimum of the conduction band.

Implementation of modulation doping via MBE can be done in 3D as bulk doping or 2D as a δ-doping plane. Delta-doping has been shown to have both significant advantages and disadvantages over bulk doping. In some cases, delta doping can lead to high electron mobilities while in other cases it is more prone to parasitic parallel conduction.

2.4 Magnetotransport

The density of states for a 2DEG was previously described for the case of zero magnetic field. However, interesting phenomena occur when the density of states is further modified by the presence of a magnetic field. The electrons occupy the quantized energy eigenvalues spaced by $\hbar\omega_c$, where ω_c is referred to as the cyclotron frequency. The name given to the discretized 2D density of states in the presence of a magnetic field is Landau Levels, depicted in figure **??**. Landau levels are the quantum mechanical equivalent of classical cyclotron orbits.

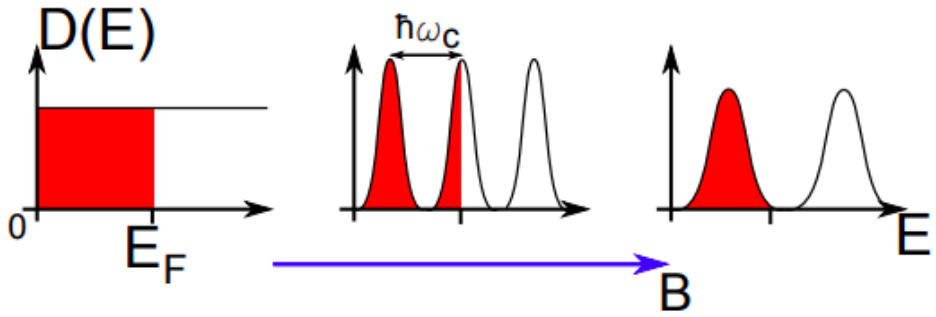

Figure 2.9: Electronic density of states of a 2DEG as a function of increasing magnetic field.

2.4.1 Quantum Hall effect

A remarkable result of the quantization of 2D density of states into Landau levels is the quantum Hall effect. In the case of a disorder free material, the Landau levels are exact delta functions spaced by $\hbar\omega_c$ with no available states in between. In this scenario, as Landau levels are depleted the Fermi level will drop instantaneously to the next Landau level. Thus, the quantized Hall resistance value will not appear in measurements as it is an instantaneous data point. In order to measure the quantum Hall resistance, *disorder* is actually needed in the sample. Disorder creates localized states in the sample that do not contribute to transport. The localized states result from potential defects in the sample that provide them with energies that lie between Landau levels. Thus, the Fermi energy can reside at these localized states within the gap. As magnetic field is increased, these localized states are depleted but no change in Hall resistance is seen due to their localized nature which prevents them from contributing to the conductance of the device. Thus, plateaus arise in the Hall resistance for a range of magnetic field values as these localized

states depopulate. The resistance of the plateau corresponds to an integer number of filled Landau levels according to

$$R_{xy} = \frac{1}{\nu}\frac{h}{e^2}, \quad \nu = 1, 2, 3, ... \tag{2.12}$$

where ν is referred to as the filling factor.

2.4.2 Shubnikov de-Haas oscillations

When the Fermi energy lies between two Landau levels the bulk conductivity is at a minimum (no available extended states) and likewise it takes a maximum when the Fermi level lies at the center of a Landau level (many available states). The longitudinal element of the resistivity matrix, $\rho = \sigma^{-1}$ is given by

$$\rho_{xx} = \frac{\sigma_{xx}}{\sigma_{xx}^2 + \sigma_{xy}^2}. \tag{2.13}$$

Therefore, the longitudinal resistivity is proportional to the longitudinal conductivity which has important implications. In the case σ_{xx} goes to zero, ρ_{xx} also goes to zero! At first glance this seems contradictory, a material cannot be both a perfect insulator and a perfect conductor at the same time. The answer is the presence of edge states. As the name implies, edge states are the extended states which reside at the edges of a sample. Thus, the resolution comes down to the existence of boundaries in real world samples. Extended states are states that extend entirely across a sample allowing them to contribute to conduction (the opposite of a localized state). Due to boundary conditions, edge states are higher in energy than extended states in the bulk. As figure **??** depicts, when the Fermi level lies between the bulk states of two Landau levels, the few higher energy edge states are the only states contributing to transport. These states do not experience backscattering since the Lorentz force from the magnetic field causes edge states located on the same edge of the sample to only have +k (or -k) states, but not both. Thus, edge states are the zero resistance states that are responsible for transport when the Fermi level resides between two Landau levels. The effects of these states are seen in the longitudinal resistance which goes to zero precisely when plateaus arise in the Hall resistance. Similarly, peaks in ρ_{xx} arise when the Fermi level resides on a Landau level corresponding to transport through bulk extended states which are subject to backscattering. These oscillations in ρ_{xx} as a function of magnetic field are known as Shubnikov de Haas oscillations (SdH).

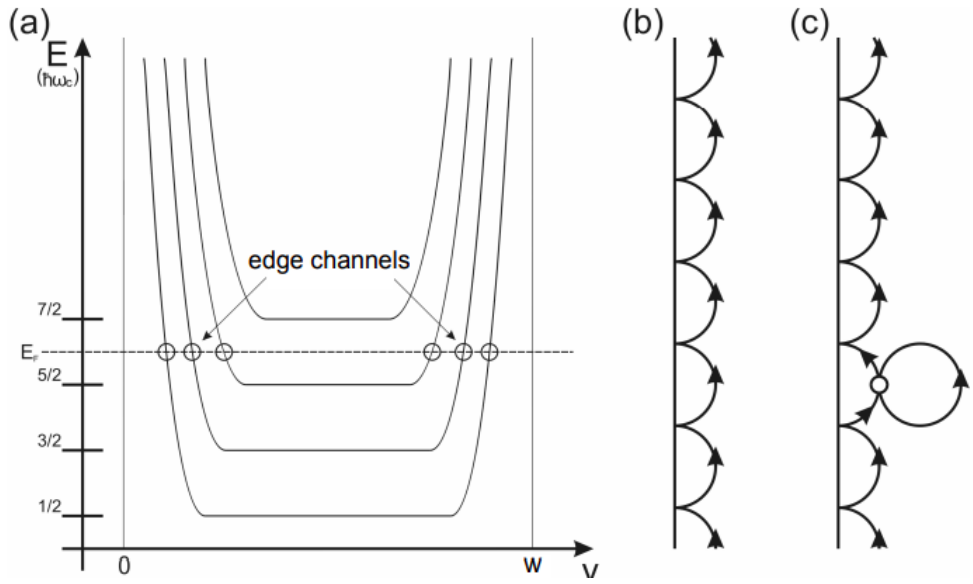

Figure 2.10: Schematic of (a) edge channels, (b) the skipping orbit of edge states, and (b) a classical view of the lack of backscattering for edge states. Reused from [**?**].

From analysis of the SdH oscillations, the carrier density of the sample can be determined. The i^{th} minima in the SdH oscillations, $i = 1, 2, 3, ...$ corresponds to i filled Landau levels. The relationship between carrier density and the number of available states is given by

$$n_s = iN_L = i\frac{eB}{h}g_s g_v \implies \frac{1}{B_i} = \frac{ig_s g_v e}{hn_s} \tag{2.14}$$

where n_s is the carrier density, i is the number of full Landau levels, and N_L is the degeneracy of states in each Landau level, g_s is spin degeneracy and g_v is valley degeneracy. From this relation, the minima of the oscillations are revealed to be periodic in $1/B$ which allows for extraction of the carrier density two or more minima in ρ_{xx} are measured. The carrier density is related to the magnetic field spacing of successive minima in resistivity by

$$n_s = g_s g_v \frac{e}{h}\left(\frac{1}{B_{i+1}} - \frac{1}{B_i}\right)^{-1}. \tag{2.15}$$

2.4.3 Temperature Dependence of Transport in 2DEGs

Measurement of the mobility of carriers in a 2DEG as a function of temperature provides a great deal of information on relevant scattering mechanisms affecting electron transport. In delta-doped III-V semiconductors, the prominent sources of scattering include interface roughness, alloy scattering, remote and background ionized impurities and lattice phonons [**?**]. Electrons moving in an applied magnetic field will experience backscattering due to these mechanisms, leading to a shortened relaxation time.

The effect of scattering on transport can be divided into two regimes, low and high temperature. At low temperature, Coulomb scattering from ionized impurities dominates. Impurity scattering can result from both remote ionized impurities and background impurities. The strength of each depend on the intentional doping of the sample. As discussed previously, modulation doping of semiconductor quantum wells leads to a drastic reduction in remote ionized impurity scattering since Coulomb scattering is a range sensitive mechanism [**?**]. Unlike impurity scattering which results from intentional doping of a material, phonon scattering originates from lattice vibrations and is unavoidable. At higher temperatures, generally above 77K, phonon scattering becomes the dominant scattering mechanism. This is signaled by a significant drop in 2DEG mobility with increasing temperature in the high temperature regime.

A measurement of the mobility as a function of temperature can therefore be used to characterize transport. Each scattering mechanism i has a characteristic lifetime, τ_i, which combine through Matthiessen's rule,

$$< \tau_p^{-1} >= \sum_i \tau_i^{-1}, \tag{2.16}$$

to give the total scattering lifetime τ_p of the system. For standard InSb quantum wells, it has been shown that the dominant mechanisms are impurity scattering from remote and background impurities (at low temperatures) and phonon scattering from both optical and acoustic phonons (at high temperatures) [**?**][**?**][**?**][**?**][**?**]. Additionally, interface roughness and intersubband scattering can play a significant role and should be considered if relevant to the system in question. Interface scattering plays a large role in systems where a significant lattice mismatch between materials strains the heterostructure as discussed previously [**?**][**?**]. Additionally, intersubband scattering affects systems with spin-splitting or carrier densities high enough to populate a second subband [**?**][**?**][**?**][**?**][**?**][**?**][**?**][**?**].

Chapter 3

Device fabrication

3.1 Introduction

All heterostructures studied in this thesis were grown by molecular beam epitaxy (MBE). The properties of InSb make it an ideal candidate for use as surface 2DEG for devices to realize Majorana Fermions. However, InSb heterostructures are far less typical in experiments compared to GaAs and InAs heterostructures and fabrication processes are much less developed. InSb is limited by its relatively low growth temperature which puts constraints on temperatures at which fabrication processes can be implemented. Additionally, there remains the question of why InSb 2DEGs suffer from low mobilities given that bulk InSb has the highest mobility of any III-V. Recent works suggest the limits on InSb mobility result from the presence of two types of crystal defects: hillocks and threading dislocations. Recent works have demonstrated success in reducing the density of defects through carefully designed buffer layers heterostructures [**?**].

The following sections of this chapter present work we did to improve the mobility and tune the carrier densities in InSb heterostructures as a pre-requisite for fabricating devices to explore topological states. Several rounds of growths were conducted to determine the ideal doping density of the heterostructure. A summary of the different growths studied in the thesis are presented in table **??**.

Summary of InSb wafer growths					
Wafer	**Type**	**Dopant**	**Doping (cm^{-2})**	**QW thickness**	**Rotation**
G381	Inverted	Te	(0.8-1.2)$\times 10^{12}$	40 nm	no
G383	Inverted	Te	(0.8-1.2)$\times 10^{12}$	40 nm	no
G387	Inverted	Te	(2.3-3.7)$\times 10^{11}$	30 nm	no
G390	Inverted	Te	(0.8-1.2)$\times 10^{11}$	30 nm	no
G396	Inverted	Te	(1.2-1.8)$\times 10^{11}$	30 nm	no
G401	Inverted	Te	(1.6-2.4)$\times 10^{11}$	40 nm	no
G414	Inverted	Te	2.6×10^{11}	30 nm	yes
G440	Standard	Si	2.6×10^{11}	30 nm	yes

Table 3.1: Summary of wafers studied for this thesis. Inverted HEMTs place the quantum well at the surface of the wafer whereas standard HEMTs bury the quantum well beneath a thick, typically n-type doped, larger band gap material. Modulation doping for all wafers is supplied by 5 tellurium (Te) or silicon (Si) δ-doping layers located 40nm beneath (inverted) or above (standard) the quantum well in an AlInSb barrier. Wafers with 30 nm quantum well (QW) thickness had a 10 nm AlInSb capping layer on top. Wafers with 40 nm quantum well thickness had no capping layer. Wafers with rotation had a uniform doping level throughout the wafer whereas wafers without rotation had a gradient of doping from one end to the other end (doping range specified in table).

3.2 Heterostructure Design

Our work focuses on inverted high electron mobility transistors (HEMTs). HEMTs result from the formation of a 2-dimensional electron gas at the interface of two semiconducting materials with differing band gaps (fig.**??**). The larger band gap material is lightly n-doped leading to band bending as the Fermi levels align to each other and form a triangular quantum well at the heterojunction (fig.**??**). In a traditional HEMT, n-type donors are located in the larger band gap material located above the quantum well or symmetrically both above and below the quantum well. Conversely, in an inverted HEMT, the lightly doped larger band gap region is located below the quantum well.

Inverted HEMTs are more difficult to achieve than standard HEMTs due to location of the quantum well nearer the surface where surface defects can strongly affect transport. In this case, the width of the top barrier plays a significant role on the mobility of the 2DEG. Additionally, the quantum well shields the doping plane from top gating preventing effective modulation of the doping density. When the doping density cannot be tuned via gating,

the proper density must be achieved during growth. As discussed later, determining the ideal doping density of a wafer can be a very time and resource-consuming process.

The inverted HEMTs studied in this thesis consist of *surface* quantum wells. These are a special case of an inverted HEMT wherein there is no top barrier. Surface quantum wells are desirable for developing topological superconductors since a suitably transparent superconductor/semiconductor (SN) interface can be achieved. However, surface quantum wells typically suffer from low mobilities due to their location at the surface of the wafer where defects and roughness are significant sources of scattering. Additionally, they are highly susceptible to surface treatment and handling during processing making fabrication more challenging than a buried 2DEG where the electronic wave function is isolated from the surface by a top barrier. In general, higher mobilities are achieved when the 2DEG is located farther from the surface.

3.2.1 InAs HEMT material

Our InAs 2DEG is a commercially supplied wafer from Intelli-Epitaxy. It sandwiches a 2nm layer of InAs between two larger bandgap InGaAs barrier layers. Due to the very thin layer of InAs, the wave function of the 2DEG extends well into the InGaAs barrier layers. As such, the quantum well practically extends to the surface and is able to make good contact with a normal or superconducting metal deposited there. This type of structure is referred as a quasi-buried 2DEG (fig. **??**).

Good contact is quantitatively characterized by near unity interface transparency. In the event of good contact, the semiconductor should inherit the properties of the superconductor through a phenomena known as proximity effect [**?**] [**?**]. Interface transparency, and consequently the presence of proximity effect, can be detected by the observation of Andreev reflections. Andreev reflections occur when an electron in a semiconductor impinges on the boundary with a superconductor and transmits as a Cooper pair into the superconductor by retro-reflecting a hole in the semiconductor. For unity interface transparency, the resistance of a superconductor-semiconductor-superconductor (SNS) device be reduced by a factor of two within the induced gap of the semiconductor thanks to the doubling of conductance by cooper pairs. When there is a boundary at the interface, such as a thin oxide layer or interface roughness, normal reflections will occur and reduce the number of Andreev reflections. A measure of the longitudinal resistance of an SNS device we fabricated as a function of source drain voltage is shown in figure **??** illustrating the induced gap due to Andreev reflection for a device with near unity interface transparency.

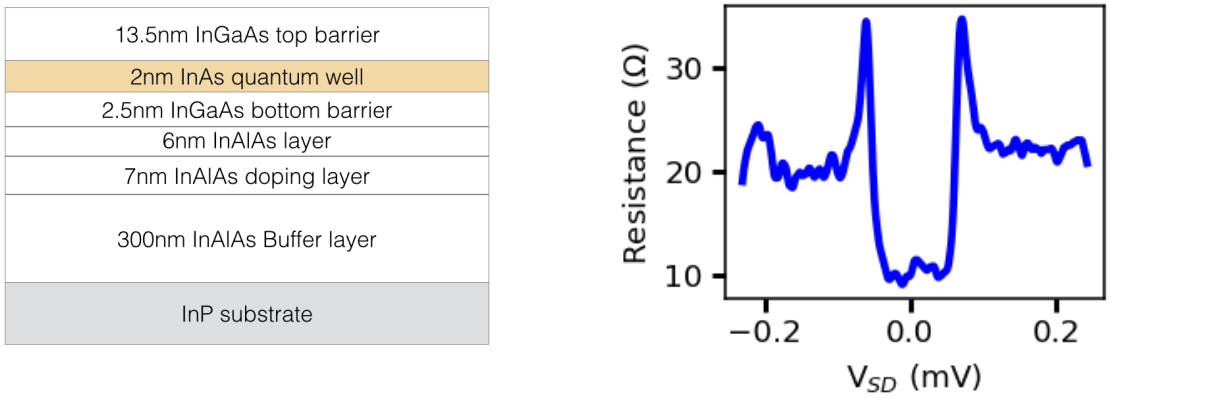

(a) (b)

Figure 3.1: (a) Schematic structure of the commercial InAs HEMT wafer used in this study. (b) Measure of longitudinal resistance versus source drain bias for an SNS device in InAs. Resistance is nearly halved within the gap, a signature of interface transparency close to unity.

3.2.2 InSb 2DEG Materials

For the InSb material system, we primarily study surface quantum wells located at the InSb/AlInSb interface 30nm below the surface of the wafer. Wafers were grown by Yinqiu Shi M.S. of the molecular beam epitaxy research group led by Dr. Zbigniew Wasilewski whom we worked in collaboration with to develop this heterostructure. Optimizing this completely new heterostructure for our needs required varying several parameters between growths.

Our buffer layer structure was optimized by the MBE team to filter the production of threading dislocations known to form at interfaces with significant lattice mismatch such as GaAs/AlSb and AlSb/GaSb. These dislocations and the surface features known as hillocks that commonly result from these dislocations are thought to be the dominant limitations on InSb quantum well mobilities. The buffer layer structure grown for the devices studied in the thesis are as follows. First, a 120 nm GaAs smoothing layer is grown on top of a GaAs (001) substrate followed by a 1 μm thick AlSb nucleation layer. The lattice constant of AlSb is halfway between GaAs and InSb and serves to reduce the lattice mismatch

between the two materials. A 5 μm GaSb nucleation cap layer is then grown to protect the AlSb below from changes in Al flux during formation of subsequent AlInSb barrier layers [**?**]. Growth of the AlInSb/InSb quantum well at this point however is not ideal due to the high density of threading dislocations at the AlSb/GaSb interface that would propagate into the quantum well. Therefore, a carefully designed buffer matrix and buffer interlayer structure is needed to filter out these dislocations. The structure designed by Y. Shi consists of three $Al_{0.12}In_{0.88}Sb/Al_{0.24}In_{0.76}Sb$ interlayers for dislocation filtering [**?**]. In addition to filtering, it was observed that for a surface off-cut angle in the range of 0.8°1.3°, threading dislocations could be reduced by a factor of 10. Furthermore, it was seen that surface hillocks originating from threading dislocations were reduced by a factor of 70.

In an extensive feedback loop with the MBE team, we varied the δ-doping density significantly resulting in wafers ranging from massively parallel conducting to non-conducting. We discovered that our ideal doping window was very narrow due to the nature of our device structure. In a top gated inverted HEMT it is difficult to gate away parallel conduction in the doping layer without pinching off the 2DEG first since the 2DEG is located between the gate and the dopant layer. In such a structure gating will bring the quantum well above the Fermi level before depleting the doping layers. Therefore, a regime must be found in which the doping layer potential is significantly shallower than the quantum well such that it depletes first despite being screened from the gate by the quantum well.

The InSb structure was designed without a top barrier since a top barrier further complicates fabrication of a proper SN interface, which requires high transparency contact to the 2DEG. In order to do this without a barrier layer, we chose a thick 30 or 40 nm InSb layer to push the quantum well at the InSb/AlInSb interface further from the surface. The design affords the well some protection from the detriments of surface scattering while also allowing the tail of the wavefunction to extend to the surface for the formation of an SN interface.

Band bending is provided by 5 Te δ-doping layers spaced 10nm apart in a AlInSb barrier layer located below the quantum well. Multiple doping layers are preferential over a single doping layer of the same total carrier density because in theory they reduce the chance of forming a parallel conduction channel. If the charge supplied by a single doping layer is dispersed into multiple layers then band bending in the doping region is reduced. As such, it's possible to achieve higher levels of total doping without risking parallel conduction. For example, one doping layer at 5×10^{11} cm^{-2} may be parallel conducting but 5 separate layers of 1×10^{11} cm^{-2} density may not be. A schematic overview of the InSb wafer structure used in this thesis and a comparison of single versus multiple doping layers is given in fig. **??**.

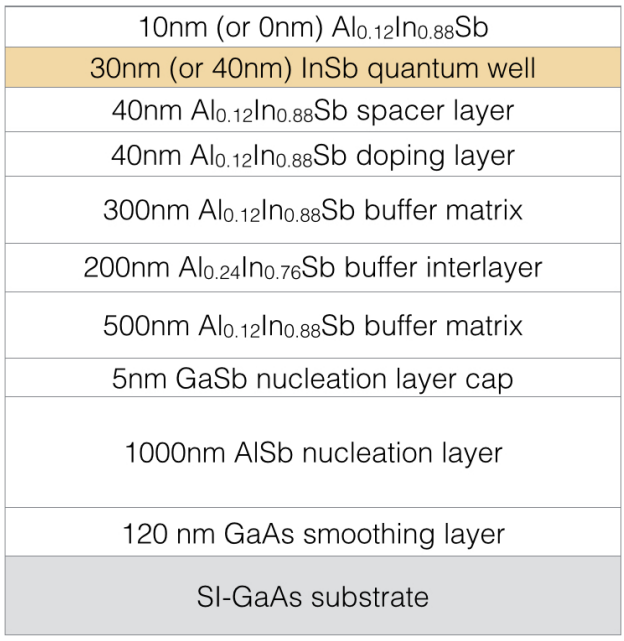

Figure 3.2: Schematic overview of the InSb surface quantum well structure studied in this thesis. The doping is provided by 5 x Te δ-doping layers spaced 10nm apart in a 40nm thick AlInSb doping layer.

3.3 Device design and fabrication

3.3.1 Hall bar

Hall bars have been fabricated using standard photo-lithography techniques discussed in the following sections. Our Hall bar design (fig. **??**) consists of 8 Ohmic contacts, three lateral Ohmics on either side of the mesa (labeled C,D,E and F,G,H) and one at each end (labeled A and B). The two end Ohmics allow current to be sent through the entire length of Hall bar while the 6 lateral Ohmics allow various combinations of voltage measurements. The pattern is designed so that the length to width ratio of the main branch of the Hall bar (boxed region in figure **??**) is $L/W = 8$. Including 6 lateral Ohmics rather than 4 allows the uniformity of the resistivity of the 2DEG to be evaluated. Measurements of resistivity of each long side of the Hall bar ($L/W = 8$) and each half of the Hall bar ($L/W = 4$) should all be equal. If they are not equivalent then the 2DEG is not spatially uniform due to impurities or other fabrication defects which affect the carrier mobility and density of

the wafer or potentially a bad (very resistive and/or includes some reactance) Ohmic is to blame. As seen in figure **??**, bonding the device to chip carriers is made easier by designing large Ti/Au bond pads off mesa (see section 3.3.2) that contact the Ohmic region of the Hall bar. Also seen in the figure is a top gate deposited on the main branch of the Hall bar. The top gate is deposited on top of a 40 nm HfO_2 layer, generally referred to as a gate oxide, to prevent leakage between the surface 2DEG and the metallic gate. The top gate allows modulation of current density within the 2DEG via applying a voltage to the top gate to accumulate or deplete carriers in the quantum well.

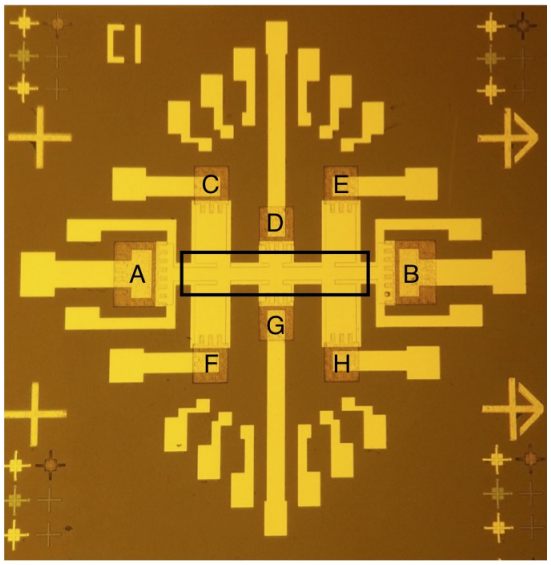

Figure 3.3: Optical image of a typical gated Hall bar device. A-H denote the 8 TiAu (yellow) Ohmic contacts of the Hall bar. Off mesa (orange) has been etched below the quantum well to be insulating. When a voltage is applied to the top gate (gold region marked by the black box), the carrier density of the 2DEG beneath is modulated. Hall bars allow measurement of the carrier density, mobility, spin orbit interaction strength, and the elastic scattering length of the 2DEG.

3.3.2 Fabrication

Mesa definition

Mesa patterns have been fabricated using standard photolithography techniques and wet etching. Photolithography is a process of patterning samples. Generally, a completed

device will undergo many stages of photolithography, one stage per etch or material deposition. Photolithography creates a stencil by exposing specific areas of a sample coated in hardened photoresist to UV light. The light shines through a glass plate patterned with chrome, known as a photo-mask, so that only areas of resist beneath windows in the photomask are exposed to light while areas beneath chrome remain in the dark (**??**). Exposure to light changes the structure of the hardened polymer. In the case of positive photoresist, UV light breaks down and weakens the long chain polymers in the resist making the exposed resist susceptible to being dissolved and washed away by UV developer (**??**). For negative resist the opposite occurs and exposed resist remains on the sample after development. Through process development, a variety of device features can be obtained using different photoresists and even combinations of photoresists. For example, our recipe for mesa definition uses a bilayer resist recipe of positive PMMA-A6 and negative maN-1410 photoresists (**??**). The bilayer recipe is desirable since PMMA-A6 provides good adhesion to the semiconductor surface while the maN-1410 is needed as a positive resist since the mesa pattern is a window (exposed) feature in our photo-mask and must remain after exposure and development. A detailed description of our fabrication process for designing Hall bars is given in appendix A and shown in figure **??**.

Ohmic contacts

Ohmics contacts are defined via a similar optical lithography process using only negative resists. A bilayer of PMGI/S1805 is used to create features with a large undercut of 1.5μm since the lateral development rate of the PMGI is faster than that of the S1805 resist (fig. **??**). The large undercut ensures that the metal layer dep"osited will be discontinuous (**??**) across the edges of the patterned Ohmics providing smooth metallic edges upon liftoff, a process in which remaining resist is dissolved in solvent after deposition and "lifts off" the undesired deposited material on top of the resist (**??**).

Recessed Ohmic contacts

For standard (non-inverted) HEMTs with buried quantum wells, a method of etching down to the quantum well surface prior to deposition is required to make good Ohmic contact. Achieving Ohmic contact is even more challenging in InSb quantum wells due to temperature constraints which prevent the use of annealing. Ion milling with ion endpoint detection has been shown to achieve good Ohmic contact without the need for a thermal anneal by terminating exactly at the surface of the quantum well [**?**].

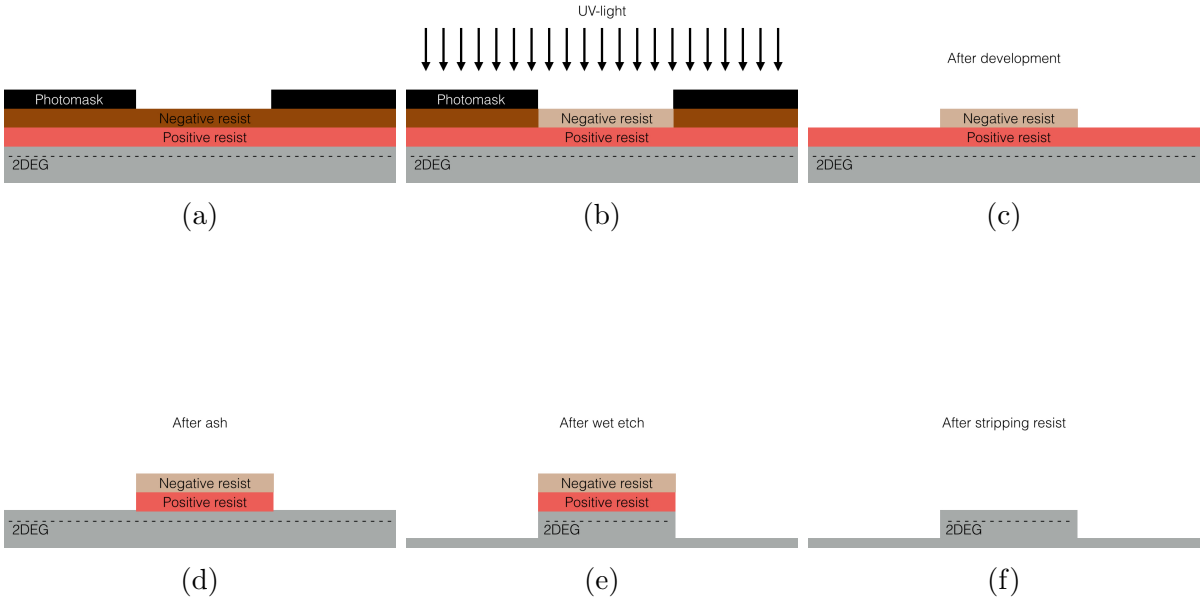

Figure 3.4: Step by step illustration of defining a mesa pattern through photolithography and wet etching. (a) Spin resist. (b) Expose. (c) Develop. (d) Ash. (e) Wet etch and (f) strip resist.

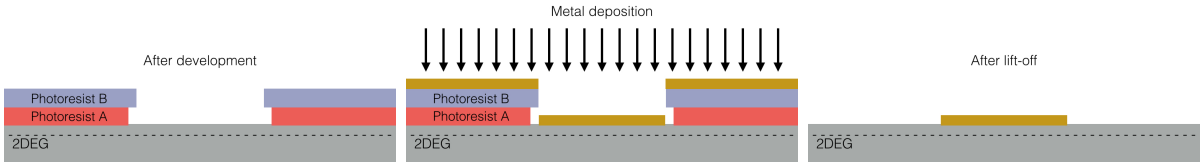

(a) (b) (c)

Figure 3.5: Step by step schematic of defining Ohmic contacts on a Hall bar device. (a) Photolithography with undercut in bilayer of photoresists with differing lateral etch rates. In the diagram, photoresist A (red, PMGI) has a faster lateral etch rate than photoresist B (blue, S1805). (b) Metal deposition (gold) of Ti/Au (20nm/100nm) by e-beam evaporation. An undercut prevents the metallic layer from being continuous, enabling metal above regions of photoresist to be easily removed. (c) Lift off of undesired metal through stripping of resist in solvent.

For buried quantum wells studied in this thesis, a wet etch down to 5nm below the quantum well surface is performed, followed by quick transfer to an Intlvac deposition system for an angular deposition of Ti/Au (20/60nm) at 45° using a rota-tilt. Given that our samples are asymmetrically doped with a delta doping layer above the quantum well, a recessed Ohmic etch removes the doping in the Ohmic region and thus depletes the quantum well below. Thus, the angular deposition allows Ti/Au to contact the corner and sidewall of the recessed area in order to make contact with the quantum well at the boundary of the Ohmic.

Summary of InSb wafer growths

Sample	**Etch depth**	**Evaporation angle)**	**R_c (kΩ)**
1	0 nm	0°	200,000
2	75 nm	0°	10,000
3	125 nm	0°	3,000
4	125 nm	45°	500
5	145 nm	45°	95
6	150 nm	45°	8

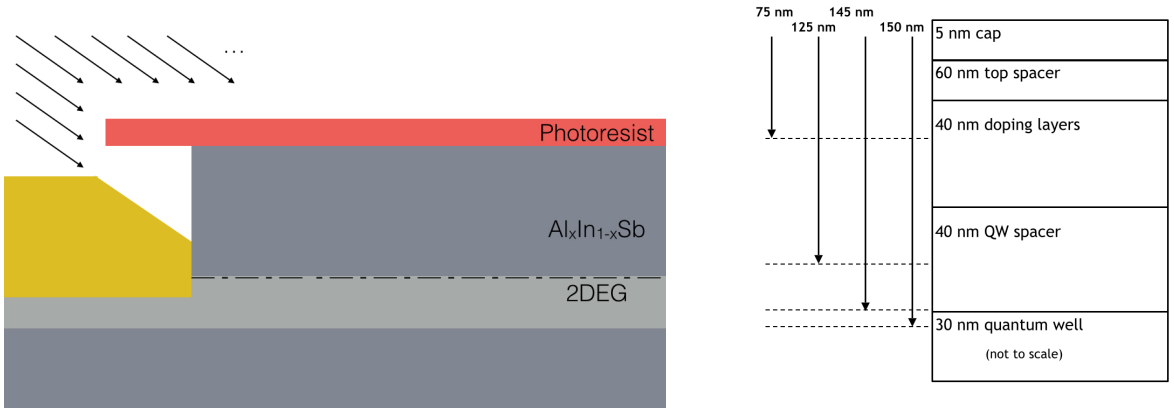

(a) (b)

Figure 3.6: Schematic diagram of (a) the structure of recessed Ohmic contacts. The mesa (dark grey) is etched down to just below the surface of the quantum well (light grey). A 45° e-beam deposition of Ti/Au (gold) makes contact with the 2DEG (dot-dashed line) along the sidewall of the etch. Undercut photoresist (red) formed from lateral etching creates an ideal structure for lift-off. (b) Diagram showing various etch depths in relation to the heterostructure as described in table **??**

Table 3.2: Summary of recessed Ohmic fabrication recipes attempted to achieve low contact resistance Ohmic contacts. The table includes the etch depth, the evaporation angle and the resulting contact resistances R_c of the Ohmic contacts to the 2DEG.

Top gate and dielectric

Atomic layer deposition (ALD) of HfO_2 is performed using an Oxford PlasmaLab System 100 FlexAl ALD at a temperature of 150°C. Deposition of HfO_2 at this temperature does not produce a perfectly crystalline deposition of HfO_2 but permits deposition of a suitable gate oxide within the thermal budget of the InSb 2DEG.

Following ALD of HfO_2, optical lithography is used to pattern vias (windows) above the Ti/Au Ohmic contacts. A single layer of Shipley 1805 photoresist is spun, exposed and developed using the same recipe as for the Shipley 1805 layer used for Ohmic contacts. A wet etch in BOE with a rate of 1nm/min is then performed to carry out the etch of the oxide layer within the vias, allowing bondpads to contact the Ohmic contacts within these

windows. Bond pads are large areas of Ti/Au located off mesa that connect to the Ohmic contacts of the device. Bond pads allow for wire-bonding of to the pins of an external chip carrier without risking damage to the on mesa (conductive areas) of the device. Once all HfO_2 is etched away within the vias, the resist used for the via pattern is stripped away using acetone and propanol. Optical lithography and metal deposition of the bond pads and top gate then follows the same protocol as described above for Ohmic contacts.

Given that our system is a top gated inverted HEMT, we discovered that it is very difficult to dope the wafer such that the 2DEG is both conductive and gate-able. We require the ability to gate the wafer such than band bending lifts the doping layers above the Fermi level without first depleting the 2DEG which lies above.

Our low temperature experiments on gated structures revealed that the conduction layer was unable to be gated to pinchoff. This result required a systematic study to be undertaken to assess the reason for failure to properly gate the 2DEG. Possible explanations include:

- Unaccounted for surface inversion 2DEG
- Trapped mobile charge in the insulator
- Overdoping

Materials like InAs and InSb are known to have surface accumulation wherein the conduction band at the surface bends below the Fermi level creating a 2DEG at the surface of the wafer were translational invariance is broken, known as a surface inversion 2DEG [**?**][**?**]. The presence of a surface accumulation 2DEG at the InSb surface screens the engineered 2DEG from the gate electric field. The addition of an AlInSb cap was shown to prevent this issue and yielded the first successful depletion of an InSb 2DEG to pinch-off [**?**]. Although surface accumulation hinders gate-ability, it produces Schottky barrier-free contact interfaces which is ideal for producing highly transparent SN interfaces. Thus the structures studied in this thesis were designed with this goal in mind.

Charge traps in the dielectric would trap or release electrons dependent on voltage sweep direction, as exploited in nonvolatile Al_2O_3 memory devices [**?**]. This effect can be ruled out by sweeping the gate and looking for hysteresis in the measured carrier density. Over-doping causes the conduction band in the doping region to fall below the Fermi level. Applying a depleting (negative) gate voltage is unable to raise the band bending of the doping layer above the Fermi level due to screening by the quantum well. As discussed in Chapter 4, we hypothesize that the primary reason for ineffective gating in our samples results from significant over doping.

Chapter 4

Transport Measurements

4.1 Measurement setup

In order to observe features such as the quantum Hall effect, it is necessary to perform measurements at low temperatures to reduce thermal fluctuations proportional to $k_B T$ where k_B is the Boltzmann constant and T is temperature. Hall bars were measured in a Janis Cryostat with a base temperature of $T = 1.4$ K. The system is equipped with a superconducting magnet with a variable field from -6 T to 6 T and a variable temperature controller allowing measurements to be performed in a temperature range 1.4 K $\leq T \leq$ 260 K. All measurements were performed using standard AC lock-in techniques with Stanford Research Systems SR830 lock-in amplifiers. All chip carriers consisted of a minimum of 12 pins to accommodate gated Hall bars. Chip carriers are mounted onto a transport probe with 24 available twisted pair DC wires fed to a Fischer connecter at the top (room temperature) end of the probe. A thermometer located on the probe near the sample continuously measures temperature. For temperature dependent measurements, a temperature set-point can be achieved by balancing heater power with He flow rate. Thermal contact between the sample and the probe is provided by the wiring. Characterization of the time it takes for the sample temperature to reach thermal equilibrium with the thermometer for this system was previously performed by Hyung Ho Kim (Tsen group, University of Waterloo) by taking measurements of sample resistance as a function of time where thermal equilibrium is confirmed by a saturation of the sample resistance.

4.1.1 Hall measurements

A measure of the carrier density and mobility of a sample is attained from Hall bar devices. The geometry of a Hall bar is shown in figure **??**. The geometry provides end Ohmic contacts for current source and drain (4 and 8) and lateral Ohmic contacts for voltage probes across both the length and width of the device (1-3 and 5-7). From a measure of the Hall voltage, V_{xy}, across the width of the 2DEG using lateral Ohmic contacts, the carrier density n is given by

$$n = \frac{IB}{V_{xy}e}. \tag{4.1}$$

The mobility μ is found from n_{tot}, the longitudinal voltage, V_{xx}, across the length of the 2DEG and the well known L/W ratio of the device geometry by

$$\mu = \frac{I(L/W)}{n_{tot}eV_{xx}}. \tag{4.2}$$

Furthermore, the longitudinal resistivity is determined from V_{xx} by

$$\rho_{xx} = \frac{dV_{xx}}{dI}\frac{W}{L}. \tag{4.3}$$

As seen, the L/W ratio of a Hall bar sample is an important aspect of the geometry since the equations above assume a rectangular geometry. Otherwise, the Hall (transverse) voltage may contain an undesired longitudinal component and vice versa. Issues with uniformity generally result from non-uniform wet etching of the mesa, potentially due to poor adhesion of photoresist. In order to check uniformity of the sample, our Hall bar geometry includes 6 rather than 4 lateral Ohmic contacts as discussed in section 3.3.1. With current sourced through the end Ohmic contacts, 6 combinations of longitudinal voltage measurements are possible. In a uniform geometry, a measure of the voltage drop across Ohmic contacts 1 and 2 should equal the voltage drop across contacts 2 and 3. These two measurements should then sum to the voltage drop across contacts 1 and 3. The same measurement is also done for the other side of the mesa using contacts 5 through 7. Additionally, the three transverse voltage probe measurements should also agree.

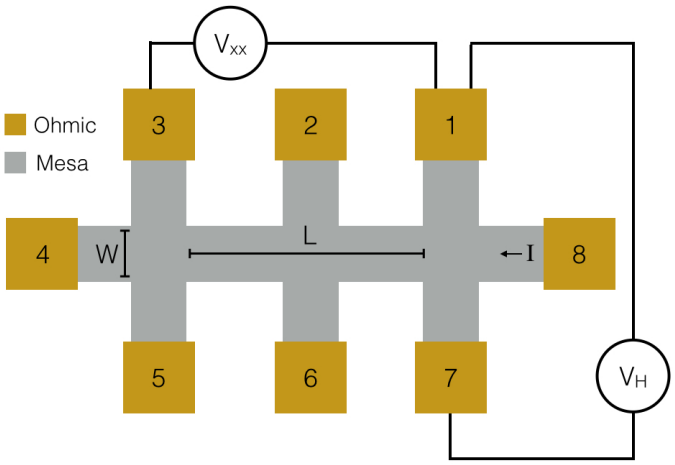

Figure 4.1: Schematic diagram of a Hall bar measurement. Lateral Ohmic contacts (1-3, 5-7) serve as the voltage probes for longitudinal (V_{xx}) and transverse (V_{xy}) voltage measurements. End Ohmic contacts (4 and 8) are used as source and drain for applying a current bias across the device.

For a measure of the SdH oscillations and quantum Hall effect, longitudinal and transverse voltages were measured using a 4-point, constant current AC measurement at low frequency (10 Hz) for a magnetic field range of 0 to 5 T. An AC signal (1V) is sent through a 1 MΩ resistor in series with the sample so that changes in sample resistance do not change the current. Limiting current to ≤ 1 μA of current reduces the effect of Joule heating which is important for measurements of SdH oscillations and the quantum Hall effect due to a reduction in oscillation amplitude with increased temperature. Data collection is controlled by our group's custom software called Spanish Acquisition. A schematic of the measurement set-up is given in figure **??**.

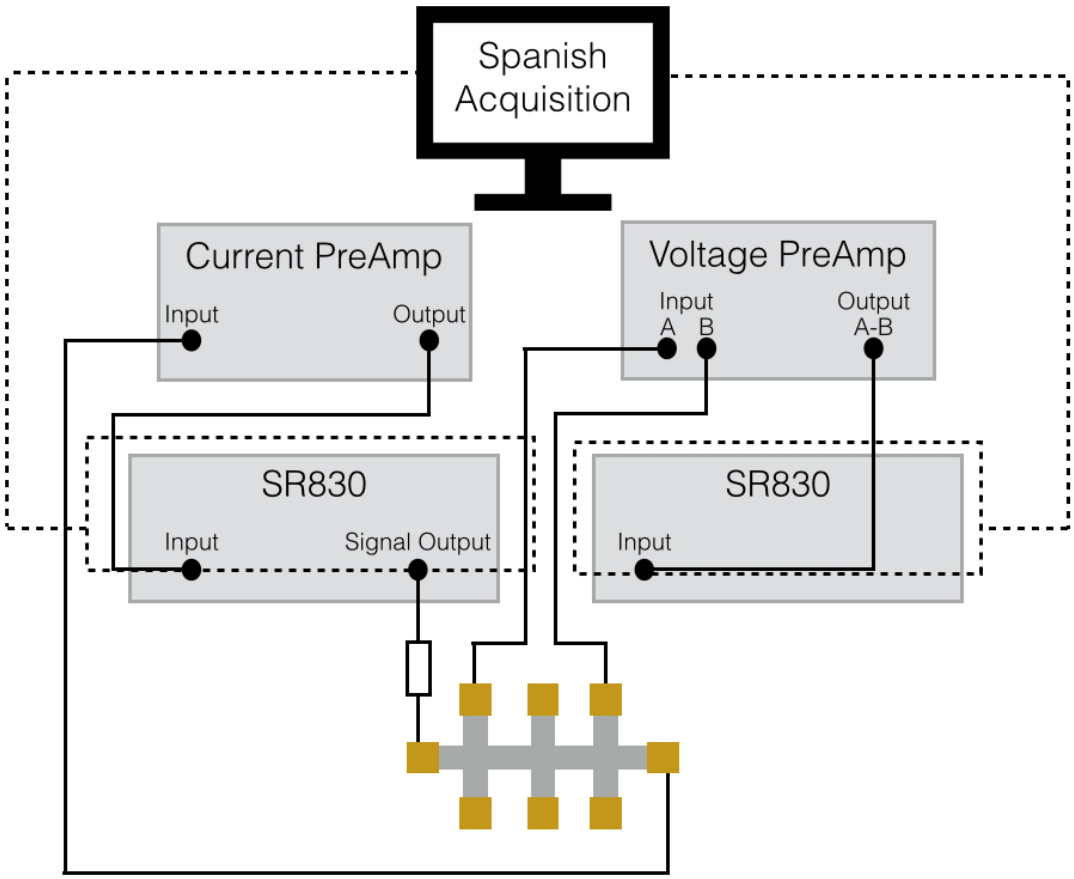

Figure 4.2: A schematic of the 4-point, constant current measurement setup used for taking longitudinal and transverse voltage measurements. A 1V AC signal is provided by the output of an SR830 lockin amplifier and sent through a 1 MΩ series resistor yielding a constant 1 μA current through the sample. Current and voltages signals pass through the input of the SR830 lockin amplifiers before being collected by Spanish Acquisition software through GPIB connections [**?**].

4.1.2 Gated measurements

The ability to modulate the carrier density of a quantum well to depletion, known as pinch-off, is of critical importance for designing devices where depletion will be used to introduce confinement, as is the case with gate defined quantum dots and quantum point contacts.

The conductive region beneath the gate is depleted by applying a negative voltage thus forming a potential barrier. The surface quantum wells we are studying must be gate-able to pinch-off in order to pursue Majorana devices where an effective 1D quantum wire will be formed in the 2DEG via top gating.

As a device reaches the pinch-off regime, the sample resistance will increase drastically as the 2DEG becomes depleted. With the constant current measurement discussed in the previous section (see fig. **??**) the device under test will quickly become significantly more resistive than the 1 MΩ resistor in series. Thus nearly the entire 1V AC signal would drop across the sample instead of the series resistor, potentially damaging the device. To prevent this from occurring, a voltage divider in place of the 1MΩ resistor will ensure only a constant small voltage is applied to the the device at all times. Thus, for gate measurements in the pinch-off regime the measurement must change from constant current to a constant voltage measurement using a voltage divider as illustrated in figure **??**. The results of gate-ability in our samples are discussed later in section 4.3.2.

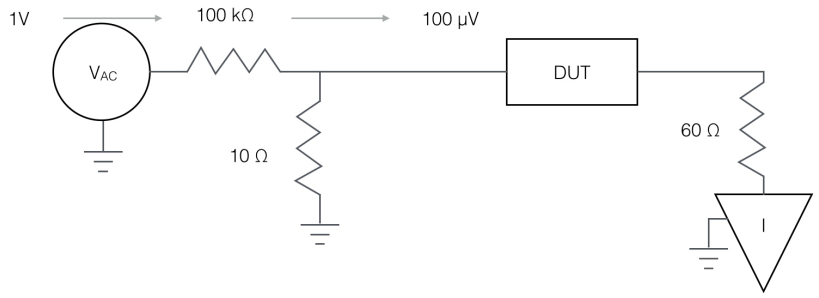

Figure 4.3: Circuit diagram of the voltage divider used in-place of the 1 MΩ resistor used in figure **??** (constant current) to perform constant voltage measurements. An AC (1V) signal is sent through a 1/10,000 voltage divider thus applying a constant 100 μV across the sample (DUT). The resistance of the shunt resistor (10 Ω in the diagram) must be much less than R_{DUT}.

4.2 Inverted InAs quantum well

Figure **??** shows the high-field magnetoresistivity (ρ_{xx}) and Hall resistivity (ρ_{xy}) of an inverted InAs quantum well sample (fig. **??**). The ρ_{xx} data exhibits distinct Shubnikov de-Haas (SdH) oscillations superimposed on top of a significant background signal, indicating the presence of a parallel conducting channel. Additionally, a noticeable beating pattern in the SdH oscillations (see figure **??** inset) indicates that there are two sets of SdH oscillations of slightly different frequency present in the sample. Given that the oscillations must be similar in frequency to induce beating, the corresponding carrier densities must be similar given the relationship of carrier density to frequency $n = (e/h)f$. The frequencies producing the nodes can be extracted through a Fourier transform of the SdH oscillation plotted as a function of $1/B$. Two frequencies were extracted from the Fourier analysis yielding carrier densities of 1.29×10^{12} cm^{-2} and 1.21×10^{12} cm^{-2}. Thus the total carrier density (n_{tot}) determined from this analysis is 2.50×10^{12} cm^{-2}. This in agreement with the measured $n_{tot} = 2.41 \times 10^{12}$ cm^{-2} from the slope of the quantum hall data where $n_{tot} = IB/eV_H$.

The beating present in similar samples has been shown to originate from either spin splitting arising from spin-orbit coupling or a second 2D subband. The origin of the beating patterns in the samples presented here was not able to be determined because we were not able to control the density via electrostatic gating. As a second subband is depleted via applying a negative top gate voltage, the decline in carrier density would influence the frequency of the second peak [**?**]. Since spin splitting results in two narrowly split bands, gating the carrier density should not strongly change the relative occupation of the bands. Gating can therefore reveal whether or not a second set of SdH oscillations results from population of a second 2D subband or spin split bands through Fourier analysis. Challenges in gating inverted HEMTs are discussed in the following section.

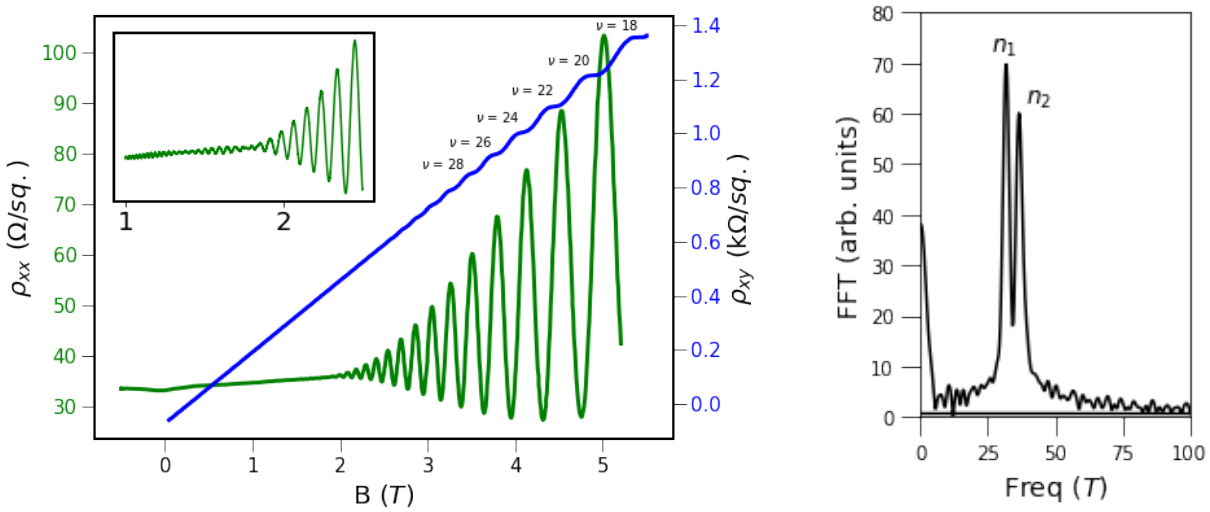

(a) (b)

Figure 4.4: (a) Longitudinal (ρ_{xx}, left axis) and transverse (ρ_{xy}, right axis) resistivity as a function of magnetic field B at $T = 1.4$K for a InAs/InAlAs heterostructure showing parallel conduction. (Inset) Low field region of ρ_{xx} indicating the onset of a beating pattering in the SdH oscillations resulting from the presence of two oscillation frequencies. (b) FFT amplitude spectrum of the sample from which the carrier densities of the two sources of SdH oscillations in the sample can be determined.

4.3 Inverted InSb quantum well

The majority of the work performed in the course of this master's thesis has been the development of an inverted HEMT, surface quantum well in InSb. These inverted structures are motivated by the need to achieve highly transparent contacts with superconductors for realizing topological states. As discussed previously, InSb quantum wells are expected to outperform InAs systems in realizing robust topological states due to properties such as its smaller electron effective mass, large Lánde g-factor and strong spin orbit coupling. However, InSb has been investigated in the community far less than other III/V systems such as GaAs/AlGaAs or InAs/InAlAs. Furthermore, inverted HEMTS are even less common, with only two known publications in literature and an InSb surface quantum well has yet to be reported. In the following sections, I present our work in optimizing both MBE growth and sample fabrication of surface quantum well samples. Below is a table

summarizing the wafers grown by Wasilewski reseach group and studied in this thesis.

Summary of InSb wafer growths				
Sample	Wafer	μ (cm^2/Vs)	n$_{2D}$ (cm^{-2})	n$_\delta$ (cm^{-2}/δ- layer)
1	G381	9.4×10^3	3.4×10^{12}	1×10^{12}
2	G383	11×10^3	2.8×10^{12}	1×10^{12}
3	G387mid	18×10^3	9.9×10^{11}	3×10^{11}
4	G387low	6.2×10^3	6.5×10^{11}	2.3×10^{11}
5	G401hi	2.7×10^3	4.4×10^{11}	2.3×10^{11}
6	G414	16×10^3	8.0×10^{11}	2.6×10^{11}
7	G414eqw	1.9×10^3	2.9×10^{11}	2.6×10^{11}
8	G440	4.8×10^3	4.0×10^{11}	2.6×10^{11}

Table 4.1: Summary by sample number and name of all InSb wafer growths including mobilities (μ), carrier densities (n_{2D}), and delta doping densities at the center of the wafer (n_δ chosen for the MBE growth for each wafer.

4.3.1 Optimization of remote ionized delta doping concentration

All wafers were grown during the same growth campaign over the course of seven weeks. By performing all growths sequentially without disturbance to the MBE chamber between growths, such as breaking vacuum, the chamber's calibrations remained constant between growths in order to only tune the delta doping concentration. Longitudinal (ρ_{xx}) and transverse (ρ_{xy}) resistivity for all growths are shown in the inset of figure **??** with doping density ranging from 2×10^{12} to 2.3×10^{11} cm^{-2} per δ doping layer. All samples show significant parallel conduction in the longitudinal resistivity, indicated by the SdH oscillations appearing superimposed on a classical parabolic background resistance. Additionally, the ρ_{xy} data sets show very little structure with no discernible quantum Hall plateau.

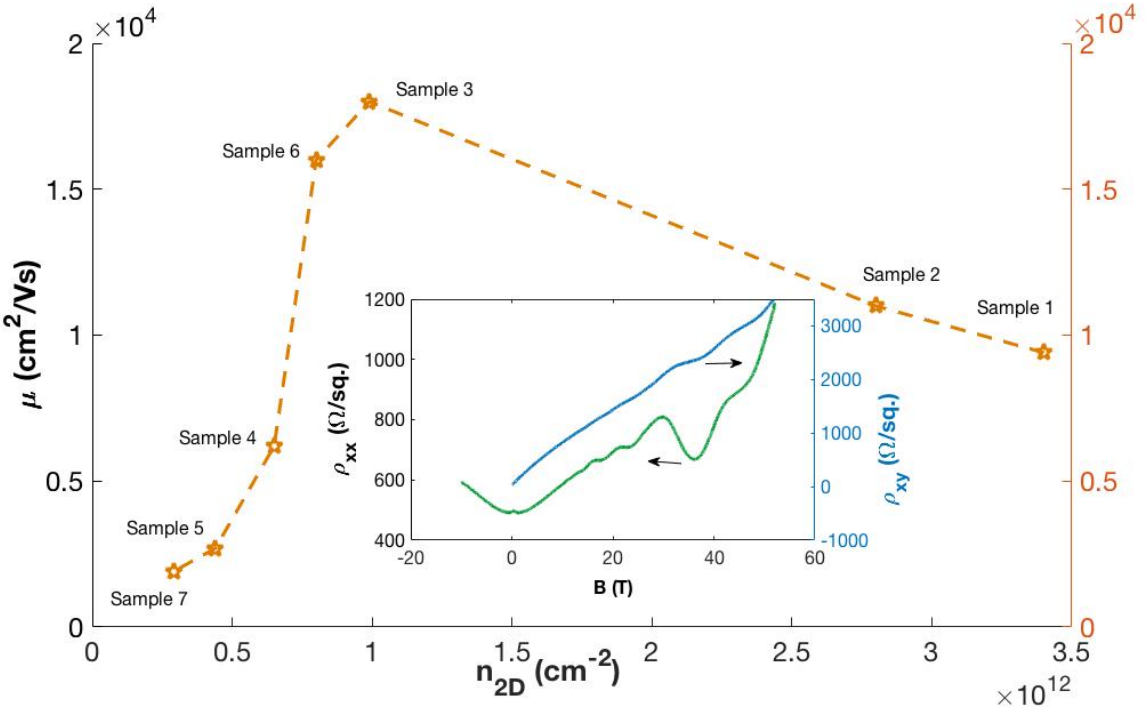

Figure 4.5: The 1.4 K mobility as a function of density for all inverted InSb HEMT samples, showing the trend in quality of each subsequent MBE growth. (Inset) ρ_{xx} (left axis) and ρ_{xy} (right axis) as a function of magnetic field B at $T = 1.4$ K for Sample 6 which is representative of the magneto-transport data for all samples. Additional data is provided in Appendix B.

As discussed in the first chapter, the quality of a 2DEG is generally quantified by the carrier mobility, but more importantly by the mobility as a function of density. For instance, a high mobility, low density sample is higher quality than a high mobility sample at higher density. A plot of mobility versus carrier density of the samples studied in this thesis is shown in figure **??**. Starting from sample 1, it can be seen that the sample quality improved as carrier density was reduced until around 1×10^{12} cm$^{-}2$. Below this threshold, the sample quality sharply declines. Recalling that the SdH data reveals parallel conduction, we hypothesize that the initial increase in mobility as density is reduced is due to having fewer low-mobility carriers in the doping plane. Below a density of 1×10^{12} cm$^{-}2$, the sharp decrease in mobility is the the result of less Thomas-Fermi screening at lower carrier densities. In this regime, further reduction in doping not only depletes the doping layer but also begins to reduce the carrier density in the quantum well reducing the

positive effects of electric field screening by the electrons in the quantum well. Without parallel conduction, the density regime between the under-doped and parallel conducting regimes would be the ideal doping regime. However, we see that the 2DEG depletes before the parallel conduction vanishes. We hypothesize that our initial doping at 1×10^{12} $cm^{-2}/\delta-$doping layer was significantly above the optimal doping level. Furthermore, we suspect that the 40nm AlInSb spacer layer between the doping layers and the quantum well is problematic. The large spacer was designed to improve 2DEG mobility by moving the 2DEG far from scattering mechanisms that plague the doping region. This is based on studies that have shown that increasing the distance between the quantum well and remote ionized doping improves the mobility of the quantum well (insert references here) up to 30 nm. Our results suggest that past 30nm the benefits of distance are outweighed by the inability to properly dope the sample.

Using nextnano3 software [**?**], self consistent Schrödinger Poisson simulations of the conduction band for wafer G414 further suggests that the InSb quantum well is not participating in transport. As seen in figure **??**, the quantum well lies 25 meV above the Fermi level, preventing population of a 2DEG. Increasing the doping density would push the conduction band of quantum well to lower energy, but with parasitic conduction already occurring in the doping region for G414, higher densities would only serve to exacerbate this issue. The solution instead would be to increase the band offset between the InSb quantum well and barrier material causing the conduction band to compensate by shifting the quantum well to lower energy. Generally, inverted HEMTs have an undoped barrier layer above the quantum well which serves this purpose. However, our goal is to eliminate the need for a top barrier. Instead, simulations show that this affect can be achieved, within reasonable alloy concentrations, with only a bottom barrier. This change is reflected in the conduction band profile by moving the quantum well to lower energy and the barrier height to higher energy to compensate for the increased offset, as seen in figure **??** for an $Al_{0.22}In_{0.78}Sb$ bottom barrier and a doping density equal to G414.

4.3.2 Effectiveness of HfO_2 as a gate dielectric on InSb

An ideal gate dielectric is one that creates a fully insulating barrier with minimal gate hysteresis from charge buildup or surface states. Recent publications have touted the success of Al_2O_3 and HfO_2 as suitable gate dielectrics for InSb [**?**][**?**]. HfO_2 has a higher dielectric constant and is able to be deposited at temperatures reportedly as low as 100° Celsius. Low temperature depositions are critically important for InSb heterostructures due to the low growth temperature of InSb and issues with dopant activation (carrier density is seen to be affected by fabrication process temperatures). HfO_2 was deposited

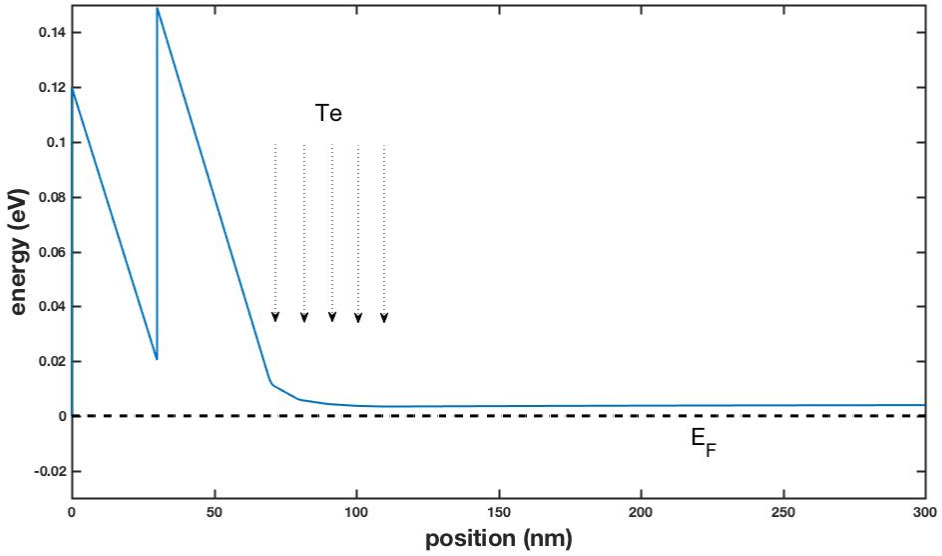

(a)

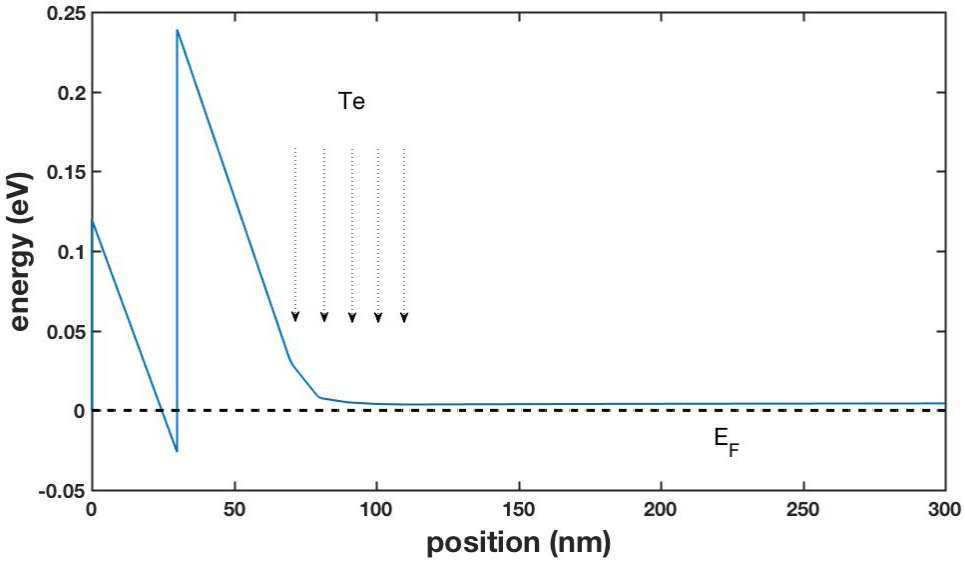

(b)

Figure 4.6: Self consistent Schrödinger Poisson simulations of the conduction band relative to the Fermi level at $E_F = 0$ eV for (a) G414 with five Tellurium (Te) δ-doped layers at $n_\delta = 2 \times 10^{11}$ cm^{-2} per δ layer and (b) a simulation of G414 with alloy concentration set to $x = 0.24$ in the $Al_xIn_{1-x}Sb$ bottom barrier and identical doping layers.

by ALD for gated surface quantum well samples. These samples were made to study the quality of our HfO_2 deposition recipe at 150° Celsius and the effectiveness of gating the carrier density of the structure. The low temperature HfO_2 ALD appeared uniform and measurements of leakage current from the gate to quantum well were negligable. The results of gating the carrier density are presented in figure **??** for sample 6.

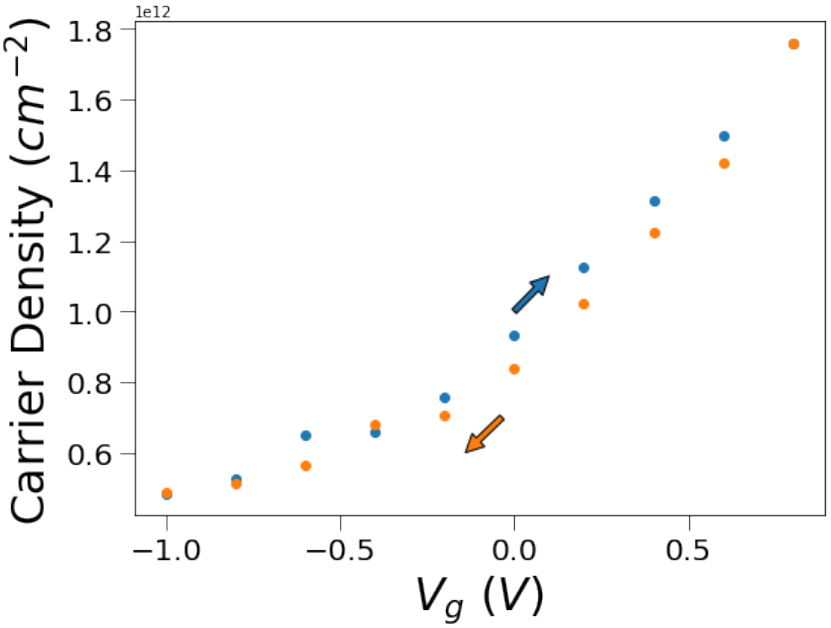

Figure 4.7: Carrier density of Sample 6 as a function of top gate voltage with sweeps from -1 V to +0.8 V and back that show minimal hysteresis in the gating.

The carrier density was modulated by a factor of three with some hysteresis an a nonlinear carrier density versus gate voltage dependence. The carrier density can be seen plateauing near 5×10^{11} cm^{-2} rendering gating to pinch-off (i.e. zero carrier density) unachievable. Currently, only two publications report achieving pinch-off in InSb systems and thus further work is still needed in improving the reliability of gated InSb samples for use in more advanced device structures [**?**][**?**].

4.4 Standard InSb quantum well

In parallel with developing surface quantum wells in InSb, we pursued studying a standard HEMT structure in collaboration with our MBE team. The MBE team is working towards eliminating the presence of hillocks and screw dislocations in InSb quantum wells [**?**]. These defects are thought to be the dominant factor limiting mobilities in InSb quantum wells and full elimination of these defects has yet to be reported. The proposed experiment for these standard structures is to compare the mobility of a wafer where hillocks are suppressed (due to offcut angle) to the wafer where hillocks are not suppressed.

A significant amount of effort was spent in developing working recessed Ohmics for this standard structure as discussed in the previous chapter. Once achieved, the wafer was characterized by magneto-transport data as previously done for the inverted structures. The ρ_{xx} and ρ_{xy} data is presented in figure **??**. Similar to previously discussed magneto-transport data, this sample shows a significant source of parallel conduction and no visible structure in the Hall data. The data from this wafer appears to be in a similar regime to the inverted structures where conduction is dominated by the parallel conducting layer. In order to study this further, a temperature dependence of the mobility of the sample was taken (figure **??**). Transport dominated by a high quality 2DEG should show mobility begin to drop at high temperatures corresponding to the onset of phonon scattering. As seen in the figure, the mobility of our sample is seen to increase as a function of temperature. This is consistent with thermally activated hopping conduction signifying that transport is dominated by a region other than the quantum well, likely due to parallel conduction in the doping layer.

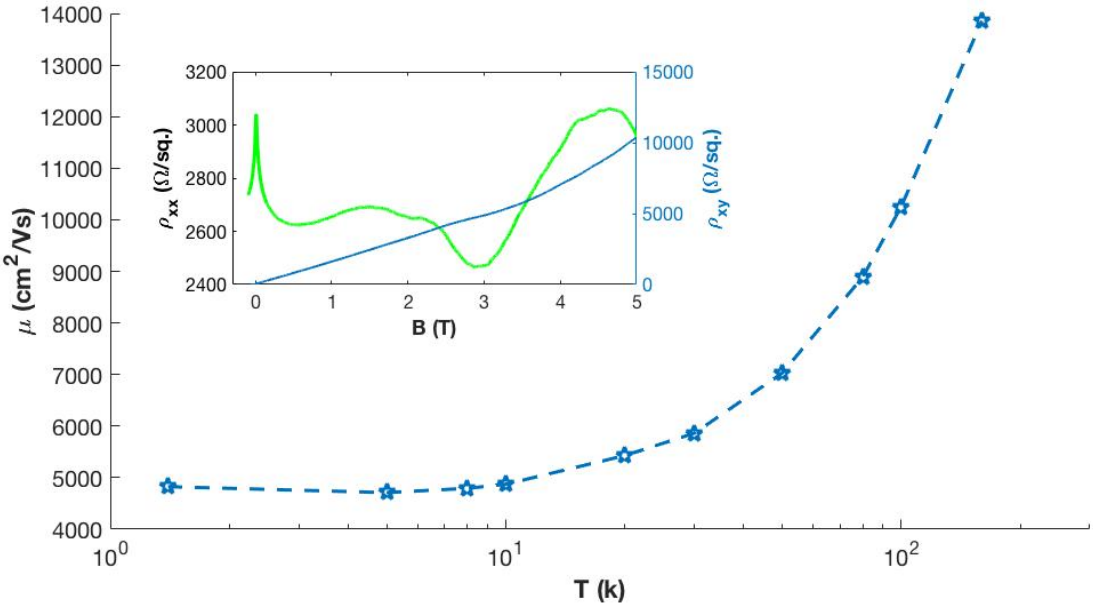

Figure 4.8: Temperature-dependent mobility of the standard InSb heterostructure exhibiting the behavior of a poor conductor rather than a 2DEG. Measurements taken from 1.4 K to 160 K. (Inset) ρ_{xx} (left axis) and ρ_{xy} (right axis) as a function of magnetic field B at $T = 1.4$ K revealing negligible structure in both data sets.

Self consistent Schrödinger Poisson simulations of the conduction band and first and second energy levels and corresponding wave functions of wafer G440 are given in figure **??**. The simulations show that band bending from the five delta doping layers at a doping density of 2.6×10^{11} cm^{-2} per delta layer brings the conduction band minima to the Fermi level, as shown by a broad, flattened minima in figure **??**. By varying the delta doping density, simulations conclude that the ideal total doping density is near 5×10^{11} cm^{-2}. Figure **??** presents the ideal bandstructure for our standard InSb HEMT heterostructure where we have reduced the number of delta-doping layers to a single delta-doping layer at a density of 5×10^{11} cm^{-2}. As seen, the single delta-doping layer creates a small dip in the conduction band profile that resides well above the fermi level.

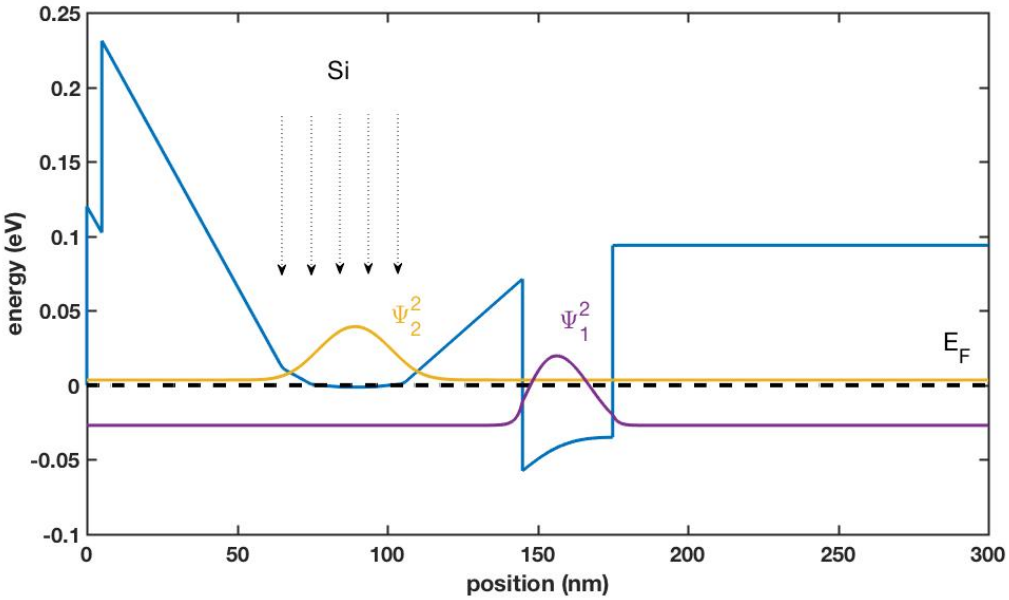

(a)

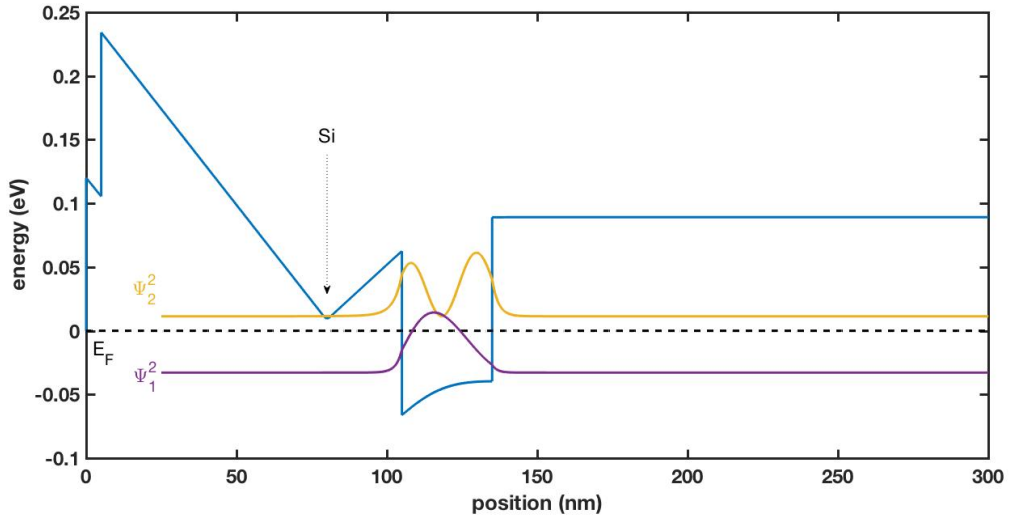

(b)

Figure 4.9: Self consistent Schrödinger Poisson simulations for (a) wafer G440 with five Si δ-doped layers at $n_\delta = 2.6 \times 10^{11}$ cm^{-2} per δ layer and (b) a wafer structure with a single delta doping layer similar to G440 but with an ideal dopant density of $n_\delta = 5 \times 10^{11}$ cm^{-2}.

Chapter 5

Summary and future work

The fabrication and transport data presented in this work for surface quantum wells in an InSb/AlInSb heterostructure has allowed us to make progress on the challenges of developing a new material system for realizing Majorana fermion devices. For the inverted structures, it was shown that a large variation in doping density, from 1.0×10^{11} to 2×10^{12} cm^{-2}, was unable to produce a useful quantum well. The SdH oscillations contained few oscillations and suffered from significant parallel conduction in the doping region for all doping densities studied. Using nextnano softaware [**?**], self-consistent Schrödinger Poisson simulations of the conduction band structure were performed and were able to show that the quantum well was not below the Fermi level. Looking forward, we will use these calculations to determine other methods of creating a proper 2DEG in this system since band bending from modulation doping was not strong enough to populate the quantum well. We've found that changes in alloy concentration of the barrier material should push the quantum well to energies beneath the Fermi level where a 2DEG will form.

For the standard HEMT heterostructure structure studied in collaboration with Wasilewski research group, we report a mobility of 4.8×10^3 cm^2/Vs and density of 4.0×10^{11} cm^{-2} for an unintentionally over-doped wafer. Simulations of the conduction band confirmed signs of overdoping in the magnetotransport data and were used to determine optimal doping densities for the next wafer growth which should eliminate this issue. We are working towards a goal of measuring the mobility in a standard InSb structure both with and without hillocks to answer the outstanding question in the field of MBE of whether or not hillocks, a type of defect in the crystal structure, are the main limitation to electron mobility in InSb 2DEGs.

Many fabrication techniques were learned and developed in working with these mate-

rials. For the surface quantum wells, techniques for low resistance Ohmic contacts and an insulating HfO_2 gate oxide were developed. For the standard HEMT, due to the lack of ion end-point detection for ion milling, we developed a method using wet-etching for making recessed Ohmics using an angular metal deposition.

Building on the conclusions of this work, the next generation of wafers should overcome the plague of parallel conduction allowing for full characterization of our carefully designed heterostructure. Characterization will include magnetotranport data for determination of quantum well mobility and density, temperature dependences of mobility and density to model the prevalent scattering mechanisms affecting transport, and effectiveness of carrier density modulation by a top gate. This, in turn, will form a strong foundation for creating devices to study topological states, such as Majorana fermions realized in 1D superconductor-semiconductor quantum wires.

References

[1] Gossard A.C. *Modulation Doping of Semiconductor Heterostructures. In: Chang L.L., Ploog K. (eds) Molecular Beam Epitaxy and Heterostructures*, volume 87 of *NATO ASI Series (Series E: Applied Sciences)*. Springer, Dordrecht, 1985.

[2] Sven Marian Albrecht, AP Higginbotham, Morten Madsen, Ferdinand Kuemmeth, Thomas Sand Jespersen, Jesper Nygård, Peter Krogstrup, and CM Marcus. Exponential protection of zero modes in majorana islands. *Nature*, 531(7593):206, 2016.

[3] AW Bett, F Dimroth, G Stollwerck, and OV Sulima. Iii-v compounds for solar cell applications. *Applied Physics A*, 69(2):119–129, 1999.

[4] Stefan Birner, Tobias Zibold, Till Andlauer, Tillmann Kubis, Matthias Sabathil, Alex Trellakis, and Peter Vogl. Nextnano: general purpose 3-d simulations. *IEEE Transactions on Electron Devices*, 54(9):2137–2142, 2007.

[5] CR Bolognesi, H Kroemer, and JH English. Interface roughness scattering in inas/alsb quantum wells. *Applied physics letters*, 61(2):213–215, 1992.

[6] James R Chelikowsky and Marvin L Cohen. Nonlocal pseudopotential calculations for the electronic structure of eleven diamond and zinc-blende semiconductors. *Physical Review B*, 14(2):556, 1976.

[7] B Das, DC Miller, S Datta, R Reifenberger, WP Hong, PK Bhattacharya, J Singh, and M Jaffe. Evidence for spin splitting in in x ga 1- x as/in 0.52 al 0.48 as heterostructures as b 0. *Physical Review B*, 39(2):1411, 1989.

[8] MT Deng, S Vaitiekėnas, Esben Bork Hansen, Jeroen Danon, M Leijnse, Karsten Flensberg, Jesper Nygård, P Krogstrup, and Charles M Marcus. Majorana bound state in a coupled quantum-dot hybrid-nanowire system. *Science*, 354(6319):1557–1562, 2016.

[9] Adam Maurick Gilbertson. *Spin and Magnetotransport Properties of Narrow Gap Semiconductors*. PhD thesis, University of London, 2009.

[10] AM Gilbertson, WR Branford, M Fearn, L Buckle, PD Buckle, T Ashley, and LF Cohen. High field magneto-transport in high mobility gated insb/inalsb quantum well heterostructures. *arXiv preprint arXiv:0903.3427*, 2009.

[11] AM Gilbertson, WR Branford, M Fearn, L Buckle, Philip Derek Buckle, T Ashley, and LF Cohen. Zero-field spin splitting and spin-dependent broadening in high-mobility insb/in 1- x al x sb asymmetric quantum well heterostructures. *Physical Review B*, 79(23):235333, 2009.

[12] AM Gilbertson, Philip Derek Buckle, MT Emeny, T Ashley, and LF Cohen. Suppression of the parasitic buffer layer conductance in insb/al x in 1- x sb heterostructures using a wide-band-gap barrier layer. *Physical Review B*, 84(7):075474, 2011.

[13] DG Hayes, CP Allford, GV Smith, Christopher McIndo, LA Hanks, AM Gilbertson, LF Cohen, Shiyong Zhang, EM Clarke, and PD Buckle. Electron transport lifetimes in insb/al1-x in x sb quantum well 2degs. *Semiconductor Science and Technology*, 32(8):085002, 2017.

[14] JP Heida, BJ Van Wees, JJ Kuipers, TM Klapwijk, and Gustaaf Borghs. Spin-orbit interaction in a two-dimensional electron gas in a inas/alsb quantum well with gate-controlled electron density. *Physical Review B*, 57(19):11911, 1998.

[15] Dmitri Iouchtchenko. Spanish acquisition [online]. URL: http://ghwatson.github.io/SpanishAcquisitionIQC/docs/.

[16] E. Kane. *Lecture notes in Narrow gap semiconductors Physics and Applications*, volume 133. Springer-Verlag, 1980.

[17] Charles Kittel, Paul McEuen, and Paul McEuen. *Introduction to solid state physics*, volume 8. Wiley New York, 1996.

[18] Ch A Lehner, T Tschirky, T Ihn, W Dietsche, J Keller, S Fält, and W Wegscheider. Limiting scattering processes in high-mobility insb quantum wells grown on gasb buffer systems. *Physical Review Materials*, 2(5):054601, 2018.

[19] TD Mishima and MB Santos. Effect of buffer layer on insb quantum wells grown on gaas (001) substrates. *Journal of Vacuum Science & Technology B: Microelectronics and Nanometer Structures Processing, Measurement, and Phenomena*, 22(3):1472–1474, 2004.

[20] Vincent Mourik, Kun Zuo, Sergey M Frolov, SR Plissard, Erik PAM Bakkers, and Leo P Kouwenhoven. Signatures of majorana fermions in hybrid superconductor-semiconductor nanowire devices. *Science*, 336(6084):1003–1007, 2012.

[21] S Nakata, K Saito, and M Shimada. Non-volatile al/sub 2/o/sub 3/memory using an al-rich structure as a charge-storing layer. *Electronics Letters*, 41(12):721–722, 2005.

[22] Fabrizio Nichele, Asbjørn CC Drachmann, Alexander M Whiticar, Eoin CT O'Farrell, Henri J Suominen, Antonio Fornieri, Tian Wang, Geoffrey C Gardner, Candice Thomas, Anthony T Hatke, et al. Scaling of majorana zero-bias conductance peaks. *Physical review letters*, 119(13):136803, 2017.

[23] J. Nieder. Magnetotransportuntersuchungen an eindimensionalen transitoren. *MPI für Festkörperforschung, Stuttgart,*, 1992.

[24] Junsaku Nitta, Tatsushi Akazaki, Hideaki Takayanagi, and Takatomo Enoki. Gate control of spin-orbit interaction in an inverted i n 0.53 g a 0.47 as/i n 0.52 a l 0.48 as heterostructure. *Physical Review Letters*, 78(7):1335, 1997.

[25] Yuval Oreg, Gil Refael, and Felix von Oppen. Helical liquids and majorana bound states in quantum wires. *Physical review letters*, 105(17):177002, 2010.

[26] JMS Orr, PD Buckle, M Fearn, CJ Storey, L Buckle, and T Ashley. A surface-gated insb quantum well single electron transistor. *New Journal of Physics*, 9(8):261, 2007.

[27] JMS Orr, AM Gilbertson, M Fearn, OW Croad, CJ Storey, L Buckle, MT Emeny, PD Buckle, and T Ashley. Electronic transport in modulation-doped insb quantum well heterostructures. *Physical Review B*, 77(16):165334, 2008.

[28] Loren Pfeiffer, KW West, HL Stormer, and KWl Baldwin. Electron mobilities exceeding 107 cm2/v s in modulation-doped gaas. *Applied Physics Letters*, 55(18):1888–1890, 1989.

[29] OJ Pooley, AM Gilbertson, PD Buckle, RS Hall, L Buckle, MT Emeny, M Fearn, LF Cohen, and T Ashley. Transport effects in remote-doped insb/alxin1-xsb heterostructures. *New Journal of Physics*, 12(5):053022, 2010.

[30] OJ Pooley, AM Gilbertson, PD Buckle, RS Hall, MT Emeny, M Fearn, MP Halsall, LF Cohen, and T Ashley. Quantum well mobility and the effect of gate dielectrics in remote doped insb/alxin1- xsb heterostructures. *Semiconductor Science and Technology*, 25(12):125005, 2010.

[31] Oliver James Pooley. *Electron Transport in InSb/AlInSb Semiconductor Heterostructures*. PhD thesis, The University of Manchester, 2011.

[32] ACH Rowe, J Nehls, RA Stradling, and RS Ferguson. Origin of beat patterns in the quantum magnetoresistance of gated inas/gasb and inas/alsb quantum wells. *Physical Review B*, 63(20):201307, 2001.

[33] TH Sander, SN Holmes, JJ Harris, DK Maude, and JC Portal. Determination of the phase of magneto-intersubband scattering oscillations in heterojunctions and quantum wells. *Physical Review B*, 58(20):13856, 1998.

[34] Thomas Schapers and Thomas Schäpers. *Superconductor/semiconductor junctions*, volume 174. Springer Science & Business Media, 2001.

[35] Y Shao, SA Solin, and LR Ram-Mohan. Carrier mobilities in delta-doped heterostructures. *arXiv preprint cond-mat/0602140*, 2006.

[36] Y Shi, D Gosselink, K Gharavi, J Baugh, and ZR Wasilewski. Optimization of metamorphic buffers for mbe growth of high quality alinsb/insb quantum structures: Suppression of hillock formation. *Journal of Crystal Growth*, 477:7–11, 2017.

[37] B Shojaei, PJJ O'Malley, J Shabani, P Roushan, BD Schultz, RM Lutchyn, C Nayak, JM Martinis, and CJ Palmstrøm. Demonstration of gate control of spin splitting in a high-mobility inas/alsb two-dimensional electron gas. *Physical Review B*, 93(7):075302, 2016.

[38] Henri J Suominen, Morten Kjaergaard, Alexander R Hamilton, Javad Shabani, Chris J Palmstrøm, Charles M Marcus, and Fabrizio Nichele. Zero-energy modes from coalescing andreev states in a two-dimensional semiconductor-superconductor hybrid platform. *Physical review letters*, 119(17):176805, 2017.

[39] Hideaki Takayanagi and Tsuyoshi Kawakami. Superconducting proximity effect in the native inversion layer on inas. *Physical review letters*, 54(22):2449, 1985.

[40] Hai Dang Trinh, Minh Thuy Nguyen, Yueh Chin Lin, Quoc Van Duong, Hong Quan Nguyen, and Edward Yi Chang. Band alignment parameters of al2o3/insb metal–oxide–semiconductor structure and their modification with oxide deposition temperatures. *Applied Physics Express*, 6(6):061202, 2013.

[41] Thomas Tschirky, Susanne Mueller, Ch A Lehner, Stefan Fält, Thomas Ihn, Klaus Ensslin, and Werner Wegscheider. Scattering mechanisms of highest-mobility inas/al x ga 1- x sb quantum wells. *Physical Review B*, 95(11):115304, 2017.

[42] MM Uddin, HW Liu, KF Yang, K Nagase, K Sekine, CK Gaspe, TD Mishima, MB Santos, and Y Hirayama. Gate depletion of an insb two-dimensional electron gas. *Applied Physics Letters*, 103(12):123502, 2013.

[43] Wei Yi, Andrey A Kiselev, Jacob Thorp, Ramsey Noah, Binh-Minh Nguyen, Steven Bui, Rajesh D Rajavel, Tahir Hussain, Mark F Gyure, Philip Kratz, et al. Gate-tunable high mobility remote-doped insb/in1- xalxsb quantum well heterostructures. *Applied Physics Letters*, 106(14):142103, 2015.

[44] Hao Zhang, Chun-Xiao Liu, Sasa Gazibegovic, Di Xu, John A Logan, Guanzhong Wang, Nick Van Loo, Jouri DS Bommer, Michiel WA De Moor, Diana Car, et al. Quantized majorana conductance. *Nature*, 556(7699):74, 2018.

APPENDICES

Appendix A

Resist recipes

Spinner settings:

Speed 5000rpm at a ramp of 1000rpm/sec for 60sec
Speed 0rpm at a ramp of 1000rpm/sec for 0sec

1. Bilayer PMGI/S1805 Recipe - Creates large undercut (for Ohmics/gate):

Bake for 1min at 180C
Spin PMGI hot
Bake 5min at 180C
Spin S1805 hot
Bake 90sec at 120C
Expose 4.5sec on Ch.2
Develop 4.5min in MF319
ASH recipe 8 (20sec)

2. Bilayer PMMA/S1811 Recipe - Creates small undercut:

Bake 5min at 150C
Spin hot Co-PMMA A6
Bake 20min at 150C
Let it cool 5min
Spin S1811
Bake 90sec at 120C

Expose 4.5sec on Ch.2
Develop 1min in MF319
ASH recipe 11 (10min)

3. Bilayer PMMA/MaN Recipe - No undercut (for mesa):

Bake 1min at 180C
Spin hot PMMA A6
Bake 5min at 180C
Let it cool 5min
Spin MaN
Bake 90sec at 110C
Expose 35sec on Ch.1
Develop 2min in MaD533s
ASH recipe 11 (10min)
Reflow bake 2min at 120C

The Hall bar fabrication process is as follows. First, we spin a layer of negative PMMA-A6 photoresist on the heterostructure using a REYNOLDSTECH-twincoater equipped with Headway Research, Inc. spinner. Spinners use centrifugal force to spread a thin uniform layer of liquid photoresist across the sample. The resist is spun at a rate of 5000rpm/s for 60s to achieve a desired thickness of approximately 600nm. The resist is hardened by a 5 minute bake at 180 Celsius then set aside to cool. A bilayer is formed by spinning a layer of positive maN-1410 photoresist on top of the hardened PMMA-A6 and is hardened by a 90 second bake at 110 Cesius.The samples are then exposed to 10.0 mW/cm^2 of UV light at 410nm for 35 seconds using a Karl Suss MA6 Aligner capable of fine lithography down to 1 micron size features. The layer of unexposed positive maN-1410 resist is developed away in MaD-533S UV developer leaving behind the exposed mesa pattern. The underlying PMMA-A6 which remains is etched away using a YES CV200-RFS O2 plasma asher via a 10 minute ash in O_2. Following etching, the sample is bare except for where the patterned maN-1410 protected the underlying PMMA-A6 from etching. A reflow bake for 2 minutes at 120 Celsius is performed to ensure good adhesion after ashing before the bare off-mesa surface area of the sample is wet etched to a depth 200 nm below the known depth of the 2DEG. In this way, the mesa remains the only conducting portion of the sample. The InAs material is wet etched in an H_2SO_4 : H_2O_2 solution and the InSb material is wet etched in a H_3PO_4 : H_2O_2 solution. The mesa etch developed for each material system is summarized in the following table.

Mesa Etch InAs					Mesa Etch InSb				
H_2SO_4	:	H_2O_2	:	H_2O	Citric Acid	:	H_3PO_4	:	H_2O_2
1	:	8	:	120	88	:	26	:	6
		45sec					35sec		

Table A.1: Recipes used for the mesa etch solution of InAs (left) and InSb (right).

In preparation for defining Ohmic contacts, the sample undergoes a 10 second dip in buffered oxide etchant (BOE) to remove any native oxide and improve surface chemistry of the sample for adhesion with photoresist. The sample is then dry baked for 1 minute at 180 Celsius and spun with PMGI while still hot at 5000rpm/s for 60 seconds. The PMGI is hardened by a 5min bake at 180 Celsius then a layer of Shipley 1805 is spun hot and hardened for 90 seconds at 120 Celsius. Using the MA6 Aligner, the Ohmic pattern is exposed with 25.0mW/cm2 of UV at 365nm-405nm for 4.5 seconds. To complete the photolithography, the exposed bilayer resist is developed in MF-319 developer for 4.5 minutes creating the Ohmic pattern with a large undercut due to the differing lateral development rates of the two resists. The large undercut ensures a successful liftoff process once metal is deposited.

Prior to deposition, the sample is descummed for 20 seconds in the YES-asher followed by a wet etch in BOE for 10 seconds to remove any native oxide on the surface for improved contact resist. The Ti/Au Ohmic contacts of thickness 20/100 nm, respectively, are then deposited in an Intlvac Nanochrome UHV-II system at a base pressure of 4×10^{-6} Torr. After deposition, the sample is placed in PG remover for a minimum of one hour before performing liftoff. This process completes the fabrication of an un-gated Hall bar device.

Appendix B

Extended Data

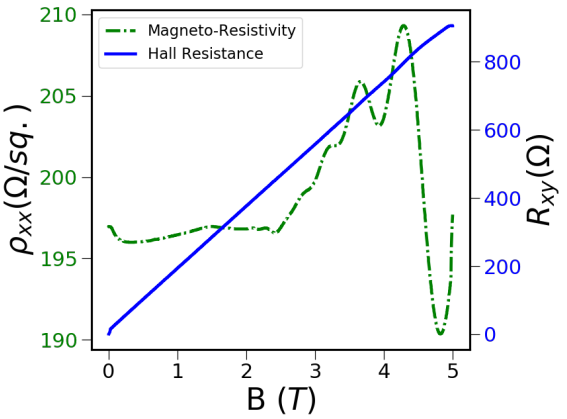

(a) Sample 1

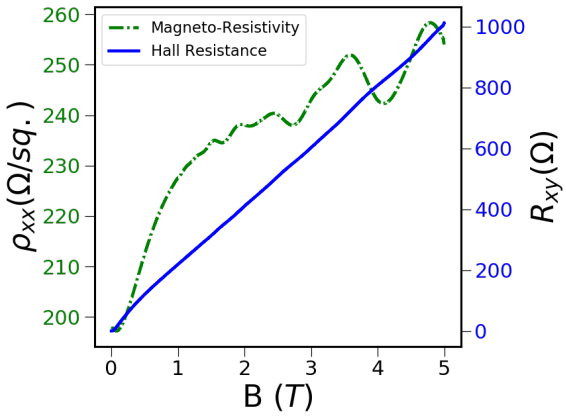

(b) Sample 2

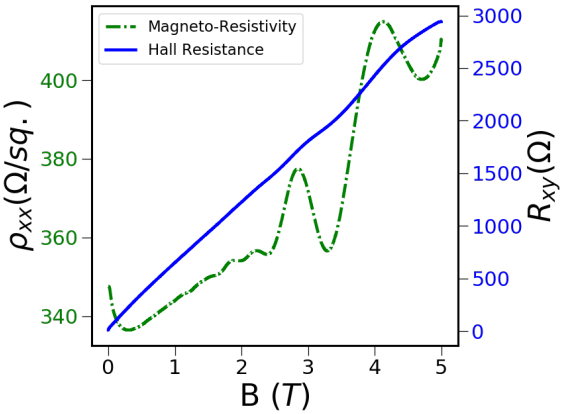

(c) Sample 3

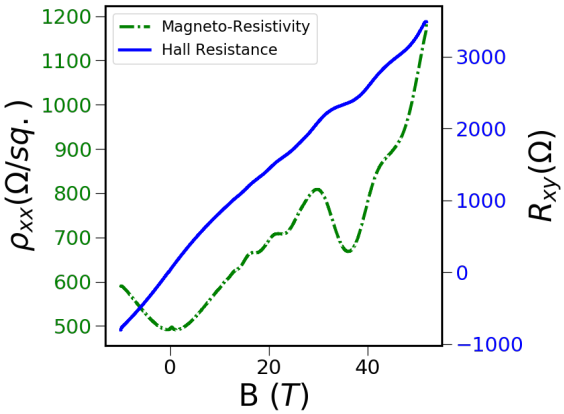

(d) Sample 6

Figure B.1: Magneto-transport data for samples studied in this work